GEOPHYSICS


10.1126/sciadv.1600581

# Diverse rupture processes in the 2015 Peru deep earthquake doublet

Lingling Ye,[1] Thorne Lay,[2]* Hiroo Kanamori,[1] Zhongwen Zhan,[1] Zacharie Duputel[3]

**Earthquakes in deeply subducted oceanic lithosphere can involve either brittle or dissipative ruptures. On 24 November 2015, two deep (606 and 622 km) magnitude 7.5 and 7.6 earthquakes occurred 316 s and 55 km apart. The first event (E1) was a brittle rupture with a sequence of comparable-size subevents extending unilaterally ~50 km southward with a rupture speed of ~4.5 km/s. This earthquake triggered several aftershocks to the north along with the other major event (E2), which had 40% larger seismic moment and the same duration (~20 s), but much smaller rupture area and lower rupture speed than E1, indicating a more dissipative rupture. A minor energy release ~12 s after E1 near the E2 hypocenter, possibly initiated by the *S* wave from E1, and a clear aftershock ~165 s after E1 also near the E2 hypocenter, suggest that E2 was likely dynamically triggered. Differences in deep earthquake rupture behavior are commonly attributed to variations in thermal state between subduction zones. However, the marked difference in rupture behavior of the nearby Peru doublet events suggests that local variations of stress state and material properties significantly contribute to diverse behavior of deep earthquakes.**

## INTRODUCTION

Seismic waves from deep earthquakes reveal the fundamental nature of rapid deformation processes in subducted oceanic lithosphere at depths of 300 to 700 km, where the great pressure should inhibit frictional sliding. The two largest recorded deep earthquakes generated seismic waves consistent with shear dislocations on one or more fault planes but had markedly different seismic radiation, indicating the existence of diverse mechanisms of strain energy release (*1*–*7*). The 9 June 1994 moment magnitude ($M_w$) 8.2 Bolivia earthquake involved an overall very slow rupture expansion speed, $V_r$, over an about 50-km-wide zone with large slip and high stress drop (*1*–*5*). In contrast, the 24 May 2013 $M_w$ 8.3 Sea of Okhotsk earthquake expanded over a region >100 km long with high $V_r$ and much lower stress drop (*5*–*7*). Radiation efficiency, a measure of radiated seismic energy relative to the available strain energy release, was very low (~0.04) for the 1994 Bolivia event and much higher (~0.6) for the 2013 Sea of Okhotsk event. Low radiation efficiency indicates a dissipative, relatively ductile source process, whereas high radiation efficiency is associated with a relatively brittle fracture process. Other large deep earthquakes have source processes that span a wide range of radiation efficiency (*8*–*15*), with thermal conditions of the subducted slab commonly assumed to influence the diversity of strain energy release. Mechanisms that have been proposed to account for deep earthquakes (source depths from 300 to 700 km) include transformational faulting triggered by metastable olivine transforming to spinel in the high deviatoric stress environment of the cold core of subducted slabs (*16*–*18*), thermal instability and runaway shear melting (*4*, *19*–*21*), dehydration embrittlement upon exsolution of a volatile component like water (*2*, *22*, *23*), or partial melting of carbonates that provides a fault-lubricating fluid.

[1]Seismological Laboratory, California Institute of Technology, Pasadena, CA 91125, USA. [2]Department of Earth and Planetary Sciences, University of California Santa Cruz, Santa Cruz, CA 95064, USA. [3]Institut de Physique du Globe de Strasbourg, Université de Strasbourg/EOST, CNRS, Strasbourg, France.
*Corresponding author. Email: tlay@ucsc.edu

## RESULTS

On 24 November 2015, a rare deep earthquake doublet occurred involving two major earthquakes (*24*) ~55 km apart separated by 316 s. The two events initiated at depths of 606 and 622 km within the subducted Nazca plate beneath eastern Peru near the border of Brazil (Fig. 1). Because seismic waves from the two events produced overlapping ground motions, we perform a two-event inversion of global low-frequency (1.67 to 10 mHz) W-phase ground motions (*25*) to estimate the individual point-source characteristics (fig. S1). Both events have predominantly double-couple normal-faulting focal mechanisms as shown in Fig. 1, compatible with shear dislocations. For the first event (E1; 22:45:38.88 UTC, 10.537°S, 70.944°W), the seismic moment $M_0$ = $2.5 \times 10^{20}$ N·m ($M_w$ 7.5) and the centroid depth $H_c$ = 611 km. For the second event (E2; 22:50:54.37 UTC, 10.060°S, 71.018°W), $M_0$ = $3.59 \times 10^{20}$ N·m ($M_w$ 7.6) and $H_c$ = 627 km. The two-event model matches the long-period waveforms well (fig. S2). We also find similar relative locations between the two events from azimuthal variation of Rayleigh wave moment-rate functions (MRFs) (fig. S3). The source centroid depths, faulting geometries, and seismic moments are similar to long-period moment tensor inversions using standard single-event processing (*24*, *26*).

Only 16 aftershocks were located during the first week after the doublet by the U.S. Geological Survey (USGS) (*24*), all with magnitudes less than 4.9, except a $M_w$ 6.7 event on 26 November 2015 located ~80 km north of the doublet at a depth of ~615 km (Fig. 1). This paucity of aftershock activity is a distinct characteristic of most deep earthquakes relative to shallow ruptures (*8*, *11*, *14*) and renders the occurrence of the large doublet all the more unusual. The earthquakes all locate within a north-south trending alignment of deep events extending from 6°S to 12°S that is well isolated from shallower seismicity in the subducted slab (fig. S4). The great 1994 Bolivia event locates about 500 km to the southeast in a region of strong slab distortion, and the 31 July 1970 ($M_w$ 8.0) Colombia deep event locates to the north in a region of very sparse activity. There have been temporally clustered pairs of large events along this deep zone in 1921–1922, 1961, 1963, 1989–1990, and 2002–2003 (fig. S4), indicating that despite the low overall seismicity levels, regional triggering interactions among large deep events are favored in this region, another common feature of deep

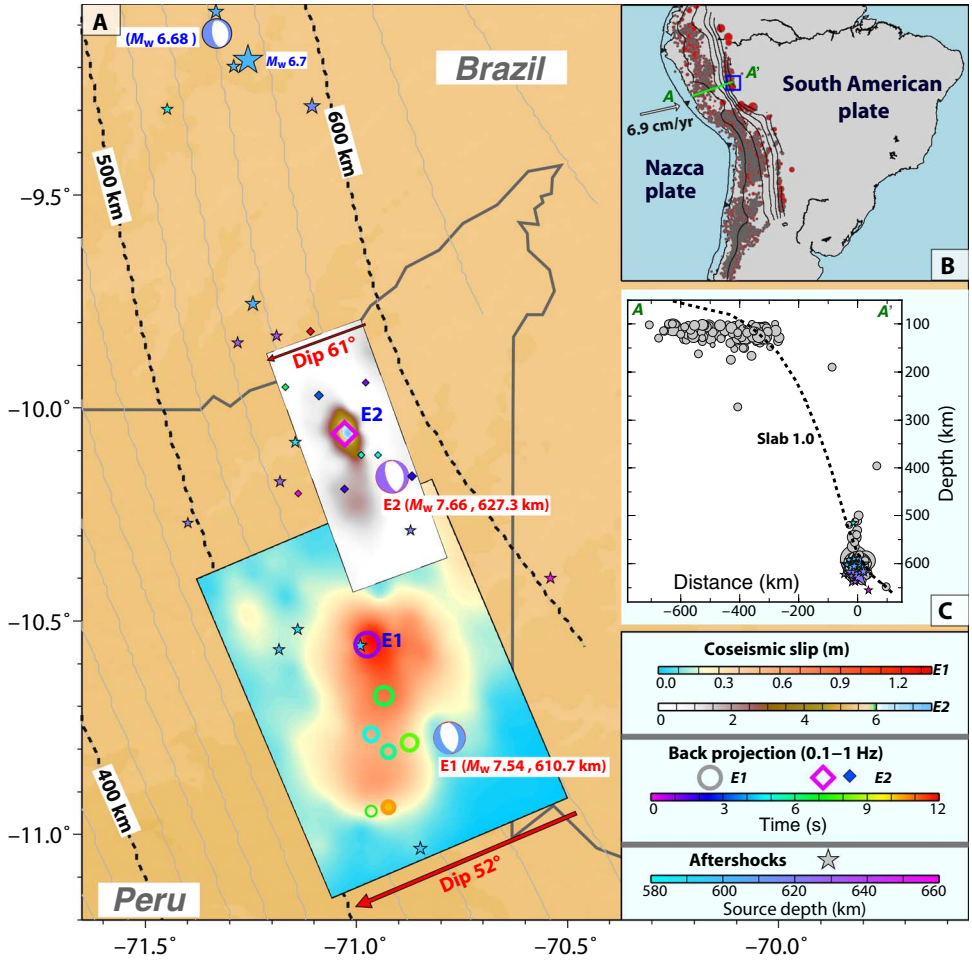


**Fig. 1. Tectonic setting of the 24 November 2015 deep Peru earthquake doublet.** (**A**) Map showing the slip distributions of the preferred rupture models (rectangles with color-coded slip models, note differences in scale) for the two events (E1, $M_w$ 7.5; E2, $M_w$ 7.7) and best double-couple faulting mechanisms from a two-event W-phase inversion for the doublet and a standard W-phase inversion for an $M_w$ 6.7 aftershock. The red arrows indicate the fault dip directions with dip angles of 52° (E1) and 61° (E2). Circles and diamonds show the locations of subevents from back-projection of global *P* waves for the 0.1- to 1.0-Hz frequency band, color-coded with time and scaled proportional to the power in the stacks for E1 and E2, respectively. Stars are locations of aftershocks with magnitudes from 4.0 to 5.1, color-coded with source depth. Contours indicate the depth of the upper surface of the deep slab from model slab 1.0 (*40*). (**B**) Plate configuration, with the Nazca plate subducting beneath the South American plate at a convergence velocity of ~6.9 cm/year. The lines are depth contours for the subducted oceanic slab, and the red dots show the seismicity with depths larger than 100 km from 1900 to 2015. (**C**) Vertical cross-section profile A-A′ from (B) with historic seismicity at along-strike distances of <150 km from A-A′ (dots), aftershocks for the 2015 Peru doublet (stars), and the upper slab surface (dashed lines).

earthquake activity (*15*, *27*). The resulting distribution of the number of events as a function of magnitude has a lower slope (*b* value ~0.3 to 0.4) than that of intermediate-depth events in the same slab (*b* value ~1.0) (fig. S5). Houston (*14*) found similar *b*-value variations and attributed them to strong thermal control on events below 300 km.

We back-project globally distributed teleseismic *P* waves in the frequency band of 0.1 to 1.0 Hz to horizontal planes at the hypocentral depths. This procedure cannot resolve minor differences in depth; thus, we emphasize the horizontal characteristics of the images. The reconstructed subevents for E1 form a southward lineation about 50 km long with seven comparable power bursts of high frequencies over about 11 s (Fig. 1), indicating $V_r$ ~4.5 km/s. In contrast, the reconstructed subevents for E2 span a limited spatial extent, with the radiation dominated by an initial large-amplitude subevent with later small subevents locating no further than ~15 km from the hypocenter (Fig. 1). We find similar patterns of subevents for the back-projections of *P* waves recorded by a large-aperture network of stations in North America and Europe (NA-EU), although the spatial resolution is not as good as for the global images. Time-integrated images of the high-frequency *P* radiation back-projected from global and NA-EU arrays for E1 and E2 (Fig. 2) show a total duration of ~20 s for both events but highlight the difference in source region dimensions of E1 and E2 for both the 0.1- to 1.0-Hz energy and the higher-frequency 0.5- to 2.0-Hz energy (fig. S6). Animations of the space-time sequence of subevents are provided in the Supplementary Materials.

The proximity of the two large events in space and time allows joint imaging of the doublet sequence using 400-s-long time windows of the *P* waves for both the northern network and the global stations,

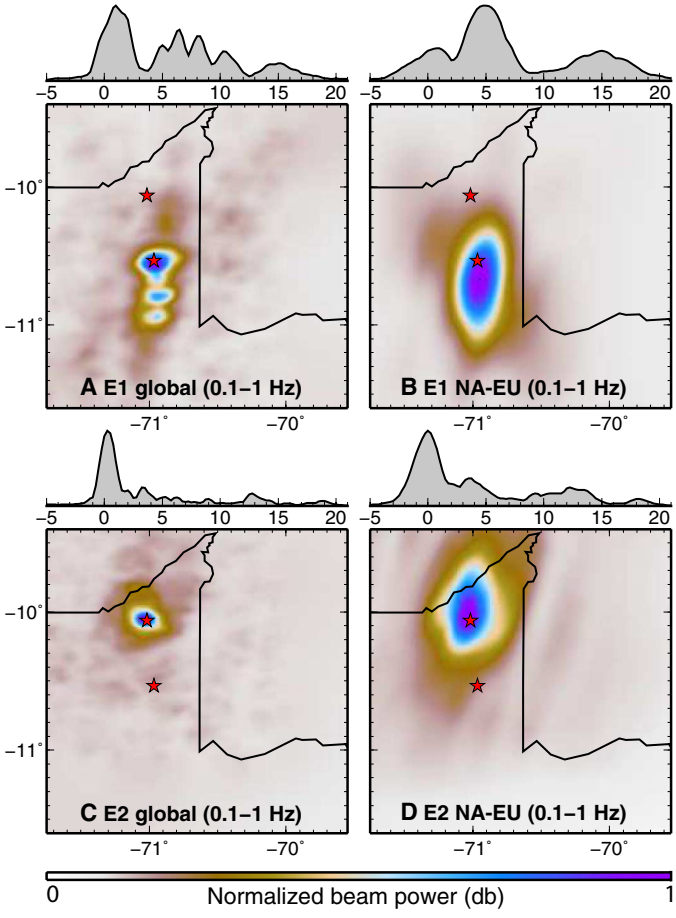


**Fig. 2. Constraints on rupture dimension and rupture velocity from *P*-wave back-projections.** (**A** to **D**) Teleseismic *P* waves in the frequency band from 0.1 to 1.0 Hz from a global distribution of stations and from NA-EU networks were used to image the coherent seismic radiation from E1 (A and B) and E2 (C and D). The time-integrated back-projected signal power over a horizontal grid around the source is shown relative to the mainshock epicenters (red stars). For E1, both global and NA-EU images indicate southward rupture extent over a distance of >50 km with a rupture propagation speed of ~4.5 km/s. Both images for E2 indicate spatially concentrated radiation without significant rupture expansion with time.

again providing relative locations of the doublet mainshocks (fig. S7). This long time window imaging can be used to identify early aftershocks in the time window between E1 and E2 by coherent high-frequency radiation bursts around the source region [none were reported by the USGS-NEIC (National Earthquake Information Center)]. We find an indication of minor energy release near the E2 hypocenter about 12 s after E1, possibly corresponding to an early aftershock dynamically triggered by *S* waves from E1 (Fig. 3 and fig. S8). Strong radiation from the E1 source region is still occurring at this time, making the detection of isolated sources difficult. We find a very clear aftershock near the E2 hypocenter about 165 s after E1 (Fig. 3 and fig. S8). The latter event is most apparent in the back-projections for the northern networks, but high-frequency *P* waves from this event are readily evident in profiles of global seismic recordings (Fig. 4), with the *P*-wave arrival time move-out being similar to that of E2 relative to E1. This demonstrates that although the rupture process of E1 involved unilateral southward rupture, activity was triggered near the hypocenter of E2 before the $M_w$ 7.6 rupture. Most aftershocks within 1 week (Fig. 1 and fig. S4) are also located to the north. The historical record shows that the slab just to the south of E1 has been aseismic during the historical period.

High-frequency back-projections place kinematic constraints on rupture processes but only image a portion of the total seismic radiation. More quantitative information about the source is provided by finite-fault slip inversions, parameterized as a space-time distribution on one or more specified fault surfaces (with geometry inferred from the long-period moment tensor inversions), with kinematics constrained by the back-projection results. We use global broadband *P* and *SH* waves (figs. S9 and S10) in finite-fault slip inversions for E1 and E2, and the resulting favored models of the slip distributions are shown in Fig. 1. Specifying $V_r$ = 4.5 km/s based on the back-projection of high-frequency subevents for E1, the corresponding slip model has peak slip of about 1.5 m, with slip extending from 10 km north of the hypocenter to 45 km south of it (Fig. 1 and fig. S11). The inversions do not resolve which of the two *P*-wave nodal planes is the actual fault plane, and there is no indication of significant vertical extent of the rupture. We slightly prefer the nodal plane dipping toward the west (strike 157°, dip 52°) because this allows directivity to sharpen some *P*-wave displacements at stations in the southern Pacific. Comparisons of observed and modeled waveforms show agreement for this model, with remarkably trapezoidal-shaped *P*-wave displacements at southern stations suggesting unilateral rupture propagation toward the south (fig. S12). These waveforms are not fit quite as well for the eastward dipping fault plane choice (fig. S13).

Although some seismograms for E2 are perturbed by the coda from E1, the data are adequate to perform finite-fault slip inversions (fig. S14). Given that the back-projections for E2 indicate concentrated energy release near the hypocenter, the constraint on rupture speed is limited. We explore a wide range of $V_r$, finding that, as $V_r$ increases, the rupture area progressively extends southward with relatively low slip but the large slip zone remains near the hypocenter (Fig. 1). Whereas the total duration of the rupture is about 20 s, the same as for E1, the waveforms of E2 have large amplitudes in the first 5 s of the *P* waves with a gradual tailing off, distinct from E1 (fig. S9). The back-projections image only high-frequency energy, but the finite-fault slip inversion would be able to resolve southward rupture extension, if it involved substantial slip. Rupture models using either west- or east-dipping nodal plane can fit the data equally well (figs. S15 and S16) because the large slip region is spatially concentrated.

We applied back-projection to the global synthetic *P* waveforms from inverted slip models for E2 with different $V_r$. All synthetic back-projections have concentrated slip near the hypocenter, but small secondary features in data back-projections are well matched by back-projections of synthetics for the slip model with $V_r$ of ~3 km/s (fig. S17). Lower $V_r$ fails to place the small bursts of energy far enough from the hypocenter, whereas higher $V_r$ positions some bursts too far south, inconsistent with the data. We slightly prefer the westward dipping fault plane (strike 160°, dip 61°), and $V_r$ = 3 km/s. This model reproduces small features near 9.9°S and 10.2°S observed in the back-projection image from the data, suggesting an upper bound of about 30 km for total fault length, but the primary slip is concentrated within an about 20-km-diameter zone (Fig. 1 and fig. S14A).

Estimates of the static stress drop for E1 and E2 from finite-fault slip models depend on the choice of $V_r$ (Fig. 5B) because $V_r$ affects the slip magnitude and spatial dimension of the source. The model for E1

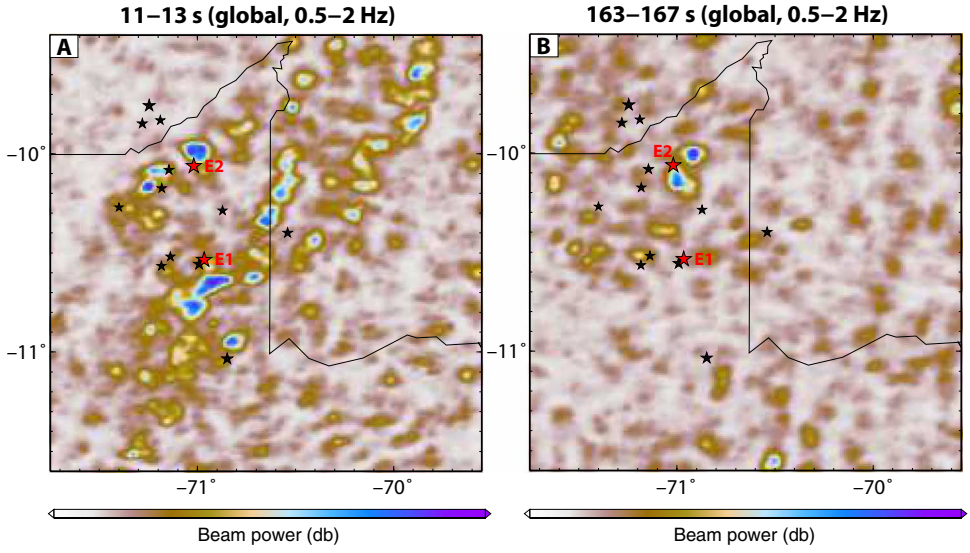


**Fig. 3. Evidence for coseismic dynamic triggering by E1 and early small earthquake at the location of E2.** (**A** and **B**) Time-integrated beam power for back-projection of 0.5- to 2-Hz teleseismic *P* waves from globally distributed broadband stations at 11 to 13 s (A) and 163 to 167 s (B). The coherent high-frequency seismic radiation near the epicenter of E2 at 11 to 13 s indicates that small rupture(s) near the location E2 might have been dynamically triggered by the *S* wave from E1. The corresponding images from the NA-EU network are shown in fig. S8. The global image has better spatial resolution for the minor energy at 11 to 13 s than that at the NA-EU network, but there is a high noise level because this time window is within the strong seismic radiation for E1 as rupture expanded toward the south. Both global and NA-EU images show coherent high-frequency radiation near the hypocenter of E2 at ~165 s after E1 and at ~150 s before E2. The red stars indicate the epicenters for E1 and E2, and the black stars indicate locations of aftershocks from the USGS/NEIC catalog.

appears to be relatively well resolved, and we estimate a slip-weighted static stress drop (*28*) of 2.3 MPa using the slip model with $V_r$ = 4.5 km/s, comparable to values for shallow interplate events. For our preferred model with $V_r$ = 3.0 km/s and 6-km grid spacing for E2, the stress drop estimate is 19.3 MPa, and this value increases very rapidly if lower $V_r$ is assumed (a common issue for concentrated ruptures with very limited resolution of spatial finiteness). We explore source models with varying spatial grid spacing to constrain bounds on the stress drop of E2. Using a 5-km grid spacing with high $V_r$ (4.5 km/s) and long subfault rupture durations gives an estimate of 15.9 MPa, whereas stress drops of about 183 MPa are found for a low $V_r$ (1.5 km/s) with 3-km grid spacing (Fig. 5B). Despite the dependence of the stress drop estimates on model parameterization, the stress drop of E2 is likely significantly larger than that of E1.

We estimate the radiated seismic wave energy, $E_R$, for E1 and E2 using teleseismic *P*-wave ground velocity recordings for the frequency range of 0.05 to 2.0 Hz, corrected for geometric spreading and anelastic attenuation (*6*, *29*). Contributions from lower frequencies are determined from the moment-rate time functions from the finite-fault inversions (*6*). For E1, we find that $E_R = 4.2 \times 10^{15}$ J, with a seismic moment–scaled value, $E_R/M_0 = 1.6 \times 10^{-5}$. For our preferred model for E2, $E_R = 7.6 \times 10^{15}$ J, and $E_R/M_0 = 2.0 \times 10^{-5}$. Thus, the radiated energy for E2 is ~80% greater than that for E1, comparable to ~45% difference in seismic moment, but the stress drop is ~8.5 times larger. The absolute values have significant uncertainty for both events, but the relative behavior is quite reliable.

The radiation efficiency, $\eta_R = \frac{2\mu}{\Delta\sigma}\frac{E_R}{M_0}$, provides important insight into the rupture physics. Unfortunately, the large uncertainties in the stress drop of E2 cause large uncertainties in $\eta_R$. Given this uncertainty, we compare $\eta_R$ for E1 and E2 as follows. The uncertainty in $\Delta\sigma$ is mainly caused by the uncertainty in the rupture speed, $V_r$. However, Ye *et al.* (*30*) showed that even if $V_r$ and $\Delta\sigma$ cannot be constrained well individually, the product $\Delta\sigma V_r^3$ can be constrained well by slip inversion, that is, $\Delta\sigma V_r^3$ is approximately constant for a given event (fig. S18). Thus, combining this with the expression for the $\eta_R$ given above, we can write $\eta_R = CV_r^3$ to a good approximation, where $C$ is a constant for a given event. (Note that the radiated energy $E_R$ is estimated mainly from the observed ground-motion velocity and depends little on the assumed $V_r$.) For E1 and E2, we determine the slip distribution with a given $V_r$ and then compute $\Delta\sigma$ and $\eta_R$. Figure 5A shows a smoothed relation between $\eta_R$ and $V_r$ thus computed for E1 and E2. The radiation efficiency, $\eta_R$, computed for E1 for our preferred rupture speed, $V_r$ = 4.5 km/s, is shown by a blue star, with a blue curve showing the variation for $V_r$ ranging from 4.0 to 5.0 km/s. The large radiation efficiency, $\eta_R$ ~1.7, could be due to stress undershoot or uncertainty in radiated energy and stress drop measurements, but it indicates a relatively brittle rupture process. Because of the larger uncertainties in $V_r$ for E2, we cannot uniquely determine $\eta_R$, but if we take the preferred value of $V_r$ = 3 km/s (with corresponding $\Delta\sigma$ = 19.3 MPa), we find $\eta_R$ = 0.2, indicated by a magenta diamond in Fig. 5A. Figure 5A also shows that, for a very large range of rupture speed, $1.5 < V_r < 4.5$, $\eta_R$ for E2 is in the range $0.03 < \eta_R < 0.75$, which is still smaller than that of E1. These results indicate that the radiation efficiency of E1 is likely significantly higher than that of E2. For comparison, Fig. 5A includes estimates for the 1994 Bolivia, the 2013 Sea of Okhotsk, and the 2015 Bonin Islands earthquakes. For the preferred value of rupture speed, 3 km/s, the radiation efficiency of E2 is between the values for the 1994 Bolivia and the 2013 Sea of Okhotsk events.

We compare source spectra and MRFs for the Peru doublet events with those of other large deep earthquakes in Fig. 6 and fig. S19. The

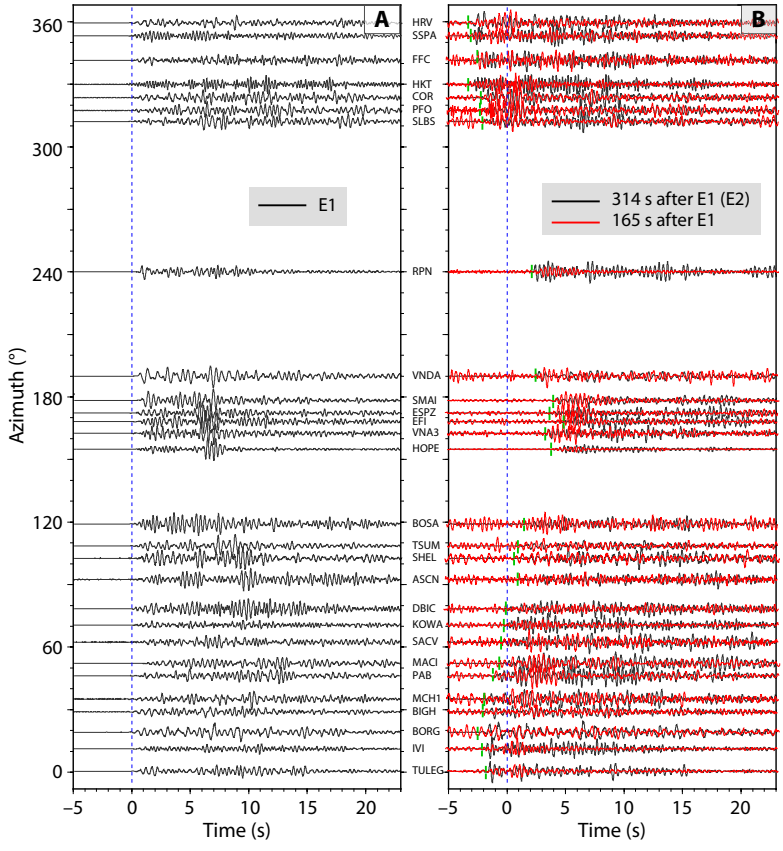


**Fig. 4. Waveform evidence of a small early aftershock near the location of E2.** (**A**) High-pass filter (>3 Hz) teleseismic *P* waves aligned on the onset of E1. (**B**) Black waveforms are for E2, aligned on the onset of E1 and shifted by 314 s. Red waveforms are similarly aligned and shifted by 165 s. The azimuthal variation of the onset of E2 (green tick marks) from the zero time corresponds to the relative location of E1, ~50 km to the north-northwest. The similar move-out of red waveforms and E2 waveforms confirms that the small event at 165 s imaged in Fig. 3 is located close to E2.

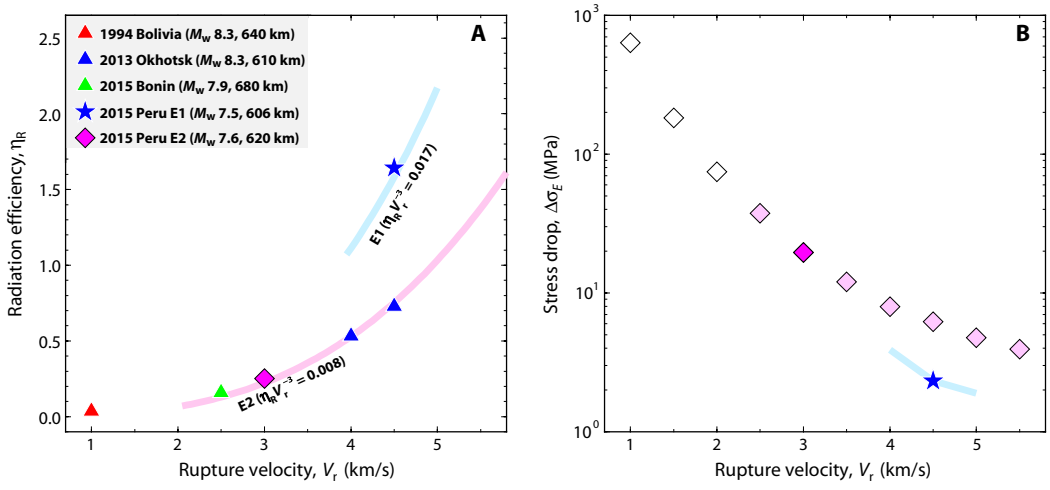


**Fig. 5. Radiation efficiency and stress drop for large deep earthquakes.** (**A**) The stars and diamonds show calculated radiation efficiency for preferred rupture models for the 2015 Peru doublet events E1 and E2, respectively. The best-fit $\eta_R V_r^{-3}$ curves from slip models with varying $V_r$ are shown as blue and purple curves within the viable $V_r$ ranges. E1 has high radiation efficiency for the favored overall rupture speed of ~4.5 km/s (blue star). Lower radiation efficiency is obtained for E2 for rupture speed of up to 5 km/s and particularly for the favored overall rupture speed of ~3 km/s (magenta diamond). Colored triangles show the estimated radiation efficiency and rupture speed for other large deep earthquakes (*4*, *6*, *15*). (**B**) Corresponding stress drops estimated from slip models with the possible $V_r$ ranges for E1 and E2. Using $V_r$ for E2 less than 2 km/s produces poor fit to minor subevents imaged by back-projection.

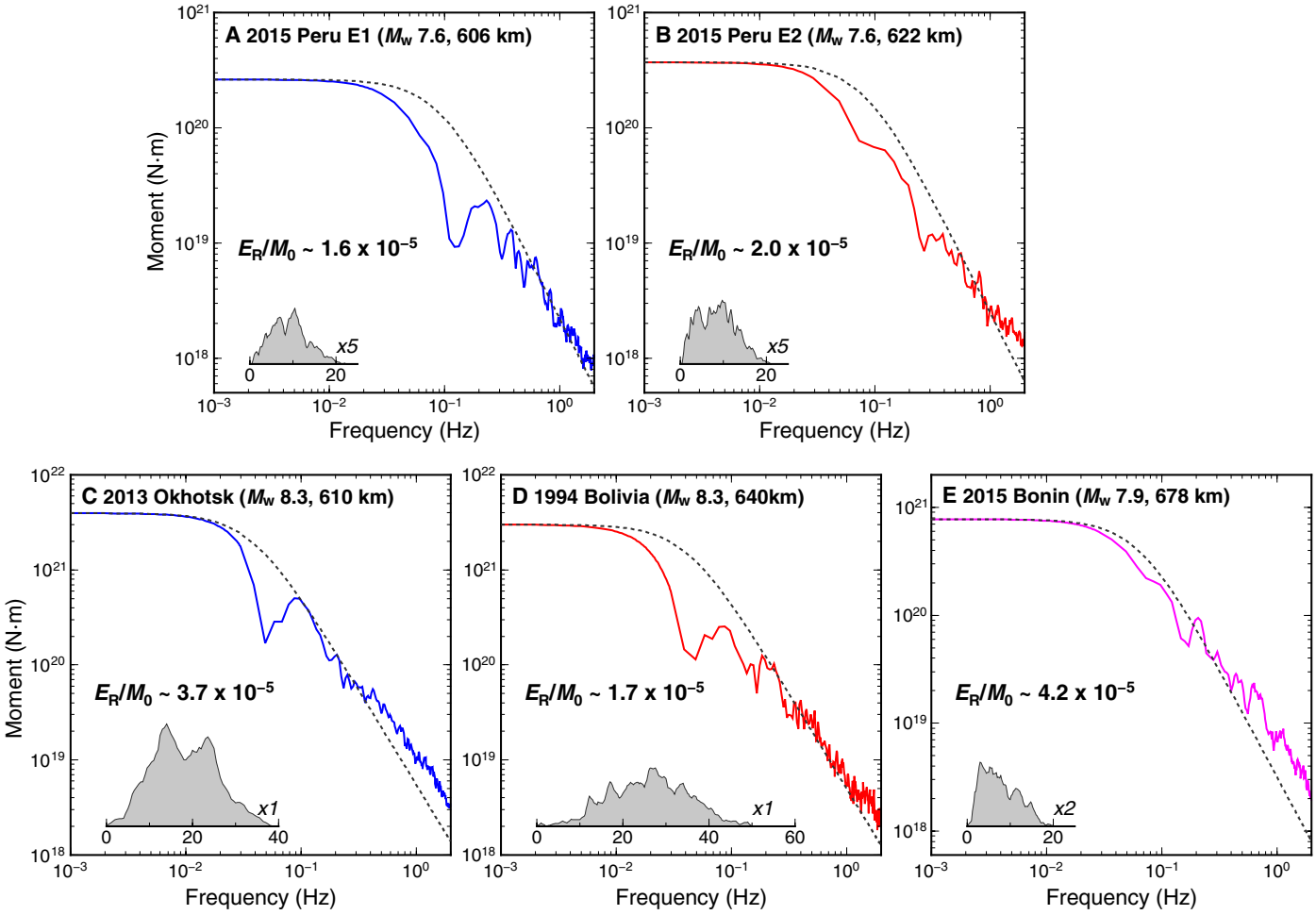


**Fig. 6. Comparison of source spectra and time functions for large deep earthquakes.** (**A** to **E**) Broadband source spectra obtained from finite-fault slip models for frequencies below 0.05 Hz and averages of propagation-corrected teleseismic *P*-wave spectra for higher frequencies (colored curves) and MRFs (inset time series) for 2015 Peru E1 (A), 2015 Peru E2 (B), 2013 Sea of Okhotsk (C), 1994 Bolivia (D), and 2015 Bonin (E) earthquakes. The dashed lines are reference $\omega^{-2}$ spectra with corresponding seismic moments, a 10-MPa stress parameter and *S*-wave velocity of 5.6 km/s. The MRFs are plotted on the same time scale with indicated variable amplitude scales. Moment-scaled radiated energy values for each event are shown.

spectra are obtained from the MRFs for frequencies below 0.05 Hz and from average *P*-wave displacement spectra corrected for propagation effects for higher frequencies. Reference point-source spectra with a 10-MPa stress parameter are shown for each event. The trough at ~0.1 Hz for E1 is a manifestation of the unilateral directivity effect on the *P*-wave ground motions. The difference in seismic efficiency between E1 and E2 is not obvious from their source spectra or source time functions, which represent only the radiated part of the released energy. The similarity in total duration of the MRFs causes the spectral shapes to be similar for E1 and E2, but this does not require similarity in stress drop. The difference in rupture speed and source area between the events estimated from back-projection images and slip distributions establishes that the stress drop of E2 is about an order of magnitude greater than that of E1.

These comparisons emphasize that we cannot fully understand the difference in the physical mechanism from only the radiated energy. To understand the source physics better, it is important to estimate the available strain energy and to investigate how much of it was radiated (*4*, *6*). For a given seismic moment, $M_0$, the available strain energy is determined by the stress drop. Thus, the difference in the stress drop between E1 and E2 estimated from back-projection images and slip distribution is the key information for distinguishing the physical mechanism of E1 and E2. Accurate estimation of stress drop requires accurate determinations of rupture area, which is especially difficult for deep earthquakes that have small source dimensions and lack near-source observations. The increased quality and data coverage of the global seismic network over time has enabled us to make increasingly reliable stress drop estimates, which enables the results presented in this study.

## DISCUSSION

The 24 November 2015 Peru deep earthquake doublet has two particularly important aspects. E1 ruptured southward with strong rupture

directivity and high $V_r$, with subevents distributed over an about 50-km rupture length. This rupture can be viewed as sequential brittle failure of several asperities on a single fault or on several fault segments. E1 appears to have dynamically activated two small aftershocks ~12 s and ~165 s later about 55 km to the north, followed by the second large event at that position, E2, which ruptured starting 316 s after E1. The doublet is the result of this delayed triggering process. The seismic moment of E2 is 40% larger than that of E1, although both have similar total rupture duration. E2 has a spatially concentrated rupture with most energy release within ~10 km of the hypocenter and minor subevents within ~15 km to the north and south. Thus, E2 has a significantly higher stress drop than E1, and radiation efficiency estimates indicate that it is also a much more dissipative rupture.

The paucity of aftershocks of both E1 and E2, and the overall low *b* value are distinct features of this region. These features are generally thought to be characteristic of materials with homogeneous strength with relatively large faults in regions where large earthquakes occur (*31*, *32*). This is in contrast to the situation in shallow seismogenic zones where many faults with various length scales exist in close-to-failure stress conditions. In regions with few aftershocks and low *b* values, an earthquake on one fault tends to occur by itself, but if faults are locally close to each other, a large failure may occasionally activate nearby faults with comparable size, resulting in doublets and clustering of earthquakes with comparable sizes. The 2015 Peru doublet and the previous clustering of big events (fig. S4) may be a manifestation of such a stress state in the subducting slab in this region.

Differences in radiation efficiency have emerged as one of the most promising probes of deep earthquake failure mechanisms, but previously reliable estimates have been made only for a few large deep events in diverse thermal environments. The Peru doublet events share a common slab environment, yet they display a large difference in radiation efficiency. This variation of behavior is even larger if the nearby 1994 Bolivia event is included in the comparison. A well-resolved feature of the 1994 event is that it began with a small initial rupture about 11 s before a large event with low rupture speed that failed in a dissipative mode. E1 is a brittle failure with normal rupture speed, whereas E2 is a rupture with lower rupture speed and lower radiation efficiency. Thus, dynamic loading because of a brittle failure appears to have played an important role in nucleating failure in a dissipative region. For the 2010 $M_w$ 6.3 deep earthquake in Spain, Bezada and Humphreys suggested (*33*) that an initial 2-MPa stress drop event was immediately followed by a much larger stress drop event. This behavior is somewhat similar to that of the 1994 Bolivia and 2015 Peru deep events.

The region near E2 could be relatively strong such that large dynamic stresses are required to nucleate failure. However, once a failure is nucleated, whether the rupture is dissipative or brittle (here, we use "brittle" to mean a rupture process with little energy dissipation) is determined by the material property and its surrounding medium condition. Higher-strength regions could fail with lower rupture speed and less radiated energy. The specific nature of the dissipative process remains unclear; it could involve a highly fractured material, melting, phase changes, or volumetric distribution of rapid deformation along a shear zone, with the volumetric damage process reducing energy available for elastic seismic radiation. Although the dynamic stresses from E1 in the Peru doublet appear to have activated the local deformation that culminated in E2, it is notable that the triggering occurred in the direction opposite to the rupture direction; thus, enhanced shaking associated with directivity was not involved. The diversity of rupture processes within the deep South American slab environment indicates that variable failure processes can occur in the same slab thermal environment. Accumulation of reliable radiation efficiency measurements for additional large deep events will shed more light on the enigmatic processes producing deep earthquakes.

## MATERIALS AND METHODS

We analyzed global seismic waves recorded by stations of the Federation of Digital Seismic Networks for all of the results presented here.

### Two-event W-phase inversion

Global long-period ground displacements in the passband of 1.67 to 10 mHz were inverted for two-event W-phase moment tensor solutions (*25*) to account for the overlapping signals. Recordings from 72 stations with a total of 93 channels were used in the inversions. Suites of hypocentral locations for both E1 and E2 were explored using a modified version of the neighborhood algorithm sampler (*34*). Figure S1 shows the hypocentral samples and the optimal best double couples for E1 and E2 at the corresponding centroid locations. For E1, the seismic moment is $2.5 \times 10^{20}$ N·m ($M_w$ 7.53) at a centroid location of 10.73°S, 71.12°W, 610.7 km depth. The centroid time shift is 8.7 s. The best double-couple fault planes have strike 354.5°, dip 44.4°, rake −74.1°, and strike 152.8°, dip 47.7°, and rake −105.0°. For E2, the seismic moment is $3.59 \times 10^{20}$ N·m ($M_w$ 7.64) at a centroid location of 10.11°S, 71.28°W, 627.3 km depth. The centroid time shift relative to the hypocentral time of E1 is 315.7 s. The best double-couple fault planes have strike 359.2°, dip 35.7°, rake −72.3°, and strike 157.7°, dip 56.2°, and rake −102.3°. The observed and synthetic waveforms for the doublet solution are shown in fig. S2.

The ground displacement waveforms were deconvolved by Rayleigh wave point-source Green's functions to determine the azimuthally varying MRFs, as shown in fig. S3. Back-projection of the Rayleigh wave MRFs for the two large events to a horizontal gridded region around the source for time intervals around their origin times was used to image their optimal centroid locations, providing additional constraint on the relative locations of the two ruptures.

### Back-projection of teleseismic *P* waves

A large number of high-quality seismic recordings from broadband stations that are distributed globally or concentrated in a large-aperture network across NA-EU provide *P*-wave signals that we back-projected to the doublet source regions to image space-time patterns of high-frequency energy release (*35*). This procedure does not assume a specific fault model or rupture speed but is only able to resolve horizontal relative positions and timing of energy bursts.

The teleseismic broadband *P* waves were aligned for E1 and E2 separately by multistation cross-correlation (*36*) and then filtered into two passbands: 0.1 to 1.0 Hz and 0.5 to 2.0 Hz. The filtered signals were then back-projected to a horizontal source region grid, with the amplitude of the fourth-root of the beam power (*35*) at each grid location in sliding time windows being determined for the global and NA-EU networks in each passband. This procedure detects coherent bursts of energy in each network, placing the source at the optimal space-time location in the grid (Fig. 2 and fig. S6). Continuous recordings 400 s long spanning E1 to E2 *P*-wave arrivals were also back-projected without separately aligning the E2 arrivals. This provided an estimate of E2 high-frequency radiation relative to the E1 hypocenter (fig. S7), along with allowing any aftershocks between the two events to be detected and located (Fig. 3 and

fig. S8). The reality of the small aftershock detection 165 s after E1 was confirmed by inspection of the waveforms (Fig. 4).

### Finite-fault slip model inversions

We used a multi–time window linear least-squares kinematic inversion procedure (*37*, *38*). The final models for E1 were parameterized with 10 nodes (central positions of subfaults) along strike and 12 nodes along dip, and those for E2 had 11 nodes along strike and 9 nodes along dip. The node spacing was proportional to the selected rupture velocity (for example, 3 km for 1.5 km/s, 6 km for 3 km/s, and 9 km for 4.5 km/s). We considered both nodal planes of the quick Global Centroid Moment Tensor (GCMT) solutions (*26*). For E1, these planes had strike 157°, dip 52° and strike 350°, dip 39°. Each subfault source time function was parameterized with fourteen 0.5-s rise time symmetric triangles with time shifts of 0.5 s, allowing subfault rupture durations of up to 7.5 s. For E2, the GCMT nodal planes had strike 160°, dip 61° and strike 350°, dip 30°, and each subfault source time function was parameterized with twelve 0.5-s rise time symmetric triangles with time shifts of 0.5 s, allowing subfault rupture durations of up to 6.5 s. Rake was allowed to vary for each triangle of each subfault by allowing two rake values ±45° from the average given by the quick GCMT solution, with a nonnegative moment constraint (*39*). The total seismic moment was constrained to match the long-period GCMT moment. The hypocenter was 600.6 km deep for E1 and 611.7 km for E2. We applied Laplacian regularization, which constrained the second-order gradient for each parameter to be zero.

Teleseismic ground displacements and ground velocities from 63 *P*-wave recordings and 49 *SH*-wave recordings for E1 and 52 *P*-wave recordings and 32 *SH*-wave recordings for E2 were used in the inversions. The data were all from global broadband seismic stations accessed through the Incorporated Research Institutions for Seismology (IRIS) Data Management Center (DMC). The data were selected from hundreds of available seismograms to have good azimuthal coverage (figs. S9 and S10) and high signal-to-noise ratios at epicentral distances from 30° to 90°. The instrument responses were removed from the raw data to recover ground displacement records. A causal bandpass filter with corner frequencies at 0.005 Hz and 1.9 Hz was applied to the data. The teleseismic Green's functions were generated with a reflectivity method that accounted for interactions in one-dimensional layered structures on both the source and the receiver sides (*38*). The Jeffreys-Bullen mantle velocity structure was used in the modeling. Signal time windows 40 s long, including 5 s of leader before the initial motion, were used.

The finite-fault solutions for E1 and E2 for the two fault planes that were considered (figs. S11 and S14) provided good overall matches to the observed global *P* and *SH* broadband ground displacements and ground velocities (figs. S12, S13, S15, and S16). We slightly prefer the solutions with westward dipping planes, but this is rather subjective, based on minor patterns in observed waveform variations. The synthetic *P* waves for the models with different $V_r$ for E2 were back-projected and compared with the data back-projections to evaluate how well the finite-source models produce minor features in the data images (fig. S17). Using rupture speed less than 2 km/s led to underprediction of the distance of secondary late features relative to the hypocenter, whereas a speed of 3 km/s matched the data well. Higher rupture speeds matched main features of the data well but produced additional small features not in the data. This indicated that 3 km/s was the most reasonable value to use for E2.

### Static stress drop estimation

Using the inverted slip models for each event, the static stress drop is calculated by

$$\Delta\sigma_E = \frac{\int_\Sigma \Delta\sigma_1 \Delta u_1 dS}{\int_\Sigma \Delta u_1 dS}$$

which is the spatial average of stress drop weighted by slip (*28*). The stress at each grid position was computed using whole-space stress relationships for the dislocations across the entire fault plane. The calculated total static stress drop values for each model are shown in figs. S11 and S14. The product $\Delta\sigma_E V_r^3$ estimated from slip models with the assumed rupture expansion $V_r$ over a range of 1.0 to 5.5 km/s are shown in fig. S18 for E1 and E2, respectively.

### Radiated energy estimation

Teleseismic broadband *P*-wave observations were analyzed for selected recordings accessed through the IRIS-DMC. Ground velocities were determined by deconvolution of the instrument responses, and the individual station measures of total radiated energy were obtained following the procedure of Venkataraman and Kanamori (*29*). We assumed $t^* = 0.35$ s as the attenuation correction for all paths. This is quite uncertain, as is the assumption of frequency-independent attenuation, but precise path-specific values are not available, and suitable empirical Green's function events are not located near the doublet events. The source spectra obtained from finite-fault MRFs were used to compute the contribution to total radiated energy for *P*-wave energy below 0.05 Hz, and logarithmic averaging of the 49 and 46 individual station measures for E1 and E2, respectively, provided the final values of $E_R$ for E1 ($4.2 \times 10^{15}$ J) and E2 ($7.6 \times 10^{15}$ J).

## SUPPLEMENTARY MATERIALS

Supplementary material for this article is available at http://advances.sciencemag.org/cgi/content/full/2/6/e1600581/DC1

fig. S1. Two–point-source W-phase inversion results for the 2015 Peru earthquake doublet.
fig. S2. Long-period waveform comparisons for the 2015 Peru earthquake doublet.
fig. S3. Rayleigh wave MRFs for the 2015 Peru earthquake doublet.
fig. S4. Historical earthquakes around the 2015 Peru deep doublet.
fig. S5. Gutenberg-Richter plots for intraslab seismicity beneath Peru.
fig. S6. Constraints on rupture dimension and rupture velocity from *P*-wave back-projections.
fig. S7. A 400-s window *P*-wave back-projection for the 2015 Peru deep doublet.
fig. S8. Evidence for coseismic dynamic triggering by E1 and early small earthquake at the location of E2.
fig. S9. Comparison of teleseismic waveforms of E1 and E2.
fig. S10. Comparison of teleseismic waveforms of E1 and E2.
fig. S11. Finite-fault slip models and shear stress changes for Peru E1.
fig. S12. Observed and predicted waveforms for E1 on the westward dipping fault plane (strike 157°).
fig. S13. Observed and predicted waveforms for E1 on the eastward dipping fault plane (strike 350°).
fig. S14. Finite-fault slip models and shear stress changes for Peru E2.
fig. S15. Observed and predicted waveforms for E2 on the westward dipping fault plane (strike 160°).
fig. S16. Observed and predicted waveforms for E2 on the eastward dipping fault plane (strike 350°).
fig. S17. Comparison of back-projections for data and synthetics from inverted slip models with different rupture speeds for E2.
fig. S18. The product of $V_r^3 \Delta\sigma_E$ for the 2015 Peru deep doublet events E1 and E2.
fig. S19. Direct comparison of seismic radiation of the 2015 Peru deep doublet events E1 and E2.

movie S1. Animation of back-projections of 0.1- to 1.0-Hz *P* waves for the global station distribution and NA-EU wide-aperture network (NA) for E1.
movie S2. Animation of back-projections of 0.1- to 1.0-Hz *P* waves for the global station distribution and NA-EU wide-aperture network (NA) for E2.

## REFERENCES AND NOTES


1. M. Kikuchi, H. Kanamori, The mechanism of the deep Bolivia earthquake of June 9, 1994. *Geophys. Res. Lett.* **21**, 2341–2344 (1994).
2. P. G. Silver, S. L. Beck, T. C. Wallace, C. Meade, S. C. Myers, D. E. James, R. Kuehnel, Rupture characteristics of the deep Bolivian earthquake of 9 June 1994 and the mechanism of deep-focus earthquakes. *Science* **268**, 69–73 (1995).
3. P. F. Ihmlé, On the interpretation of subevents in teleseismic waveforms: The 1994 Bolivia deep earthquake revisited. *J. Geophys. Res.* **103**, 17919–17932 (1998).
4. H. Kanamori, D. L. Anderson, T. H. Heaton, Frictional melting during the rupture of the 1994 Bolivian earthquake. *Science* **279**, 839–842 (1998).
5. Z. Zhan, H. Kanamori, V. C. Tsai, D. V. Helmberger, S. Wei, Rupture complexity of the 1994 Bolivia and 2013 Sea of Okhotsk deep earthquakes. *Earth Planet. Sci. Lett.* **385**, 89–96 (2014).
6. L. Ye, T. Lay, H. Kanamori, K. D. Koper, Energy release of the 2013 $M_w$ 8.3 Sea of Okhotsk earthquake and deep slab stress heterogeneity. *Science* **341**, 1380–1384 (2013).
7. Y. Chen, L. Wen, C. Ji, A cascading failure during the 24 May 2013 great Okhotsk deep earthquake. *J. Geophys. Res.* **119**, 3035–3049 (2014).
8. D. A. Wiens, J. J. McGuire, The 1994 Bolivia and Tonga events: Fundamentally different types of deep earthquakes? *Geophys. Res. Lett.* **22**, 2245–2248 (1995).
9. M. Antolik, D. Dreger, B. Romanowicz, Finite fault source study of the great 1994 deep Bolivia earthquake. *Geophys. Res. Lett.* **23**, 1589–1592 (1996).
10. L.-R. Wu, W.-P. Chen, Rupture of the large ($M_w$ 7.8), deep earthquake of 1973 beneath the Japan Sea with implications for seismogenesis. *Bull. Seismol. Soc. Am.* **91**, 102–111 (2001).
11. R. Tibi, G. Bock, D. A. Wiens, Source characteristics of large deep earthquakes: Constraint on the faulting mechanism at great depths. *J. Geophys. Res.* **108**, 2091 (2003).
12. L. M. Warren, P. G. Silver, Measurement of differential rupture durations as constraints on the source finiteness of deep-focus earthquakes. *J. Geophys. Res.* **111**, B06304 (2006).
13. Z. Zhan, D. V. Helmberger, H. Kanamori, P. M. Shearer, Supershear rupture in a $M_w$ 6.7 aftershock of the 2013 Sea of Okhotsk earthquake. *Science* **345**, 204–207 (2014).
14. H. Houston, Earthquake seismology: Deep earthquakes, in *Treatise on Geophysics* (Elsevier, Oxford, ed. 2, 2015), vol. 4, pp. 329–354.
15. L. Ye, T. Lay, Z. Zhan, H. Kanamori, J.-L. Hao, The isolated ~680 km deep 30 May 2015 $M_W$ 7.9 Ogasawara (Bonin) Islands earthquake. *Earth Planet. Sci. Lett.* **433**, 169–179 (2016).
16. H. W. Green II, H. Houston, The mechanics of deep earthquakes. *Ann. Rev. Earth Planet. Sci.* **23**, 169–213 (1995).
17. S. H. Kirby, S. Stein, E. A. Okal, D. C. Rubie, Metastable mantle phase transformations and deep earthquakes in subducting oceanic lithosphere. *Rev. Geophys.* **34**, 261–306 (1996).
18. H. W. Green II, Shearing instabilities accompanying high-pressure phase transformations and the mechanics of deep earthquakes. *Proc. Natl. Acad. Sci. U.S.A.* **104**, 9133–9138 (2007).
19. D. T. Griggs, D. W. Baker, The origin of deep-focus earthquakes, in *Properties of Matter Under Unusual Conditions*, H. Mark, S. Fernbach, Eds. (Interscience, New York, 1969), pp. 23–42.
20. M. Ogawa, Shear instability in a viscoelastic material as the cause of deep focus earthquakes. *J. Geophys. Res.* **92**, 13801–13810 (1987).
21. S.-i. Karato, M. R. Riedel, D. A. Yuen, Rheological structure and deformation of subducted slabs in the mantle transition zone: Implications for mantle circulation and deep earthquakes. *Phys. Earth Planet. Inter.* **127**, 83–108 (2001).
22. S. Omori, T. Komabayashi, S. Maruyama, Dehydration and earthquakes in the subducting slab: Empirical link in intermediate and deep seismic zones. *Phys. Earth Planet. Inter.* **146**, 297–311 (2004).
23. C. Meade, R. Jeanloz, Deep-focus earthquakes and recycling of water into the Earth's mantle. *Science* **252**, 68–72 (1991).
24. U.S. Geological Survey, http://earthquake.usgs.gov/earthquakes/eventpage/us100040ww#general_summary.
25. Z. Duputel, H. Kanamori, V. C. Tsai, L. Rivera, L. Meng, J.-P. Ampuero, J. M. Stock, The 2012 Sumatra great earthquake sequence. *Earth Planet. Sci. Lett.* **351–352**, 247–257 (2012).
26. Global Centroid Moment Tensor, www.globalcmt.org/CMTsearch.html.
27. R. Tibi, D. A. Wiens, H. Inoue, Remote triggering of deep earthquakes in the 2002 Tonga sequences. *Nature* **424**, 921–925 (2003).
28. H. Noda, N. Lapusta, H. Kanamori, Comparison of average stress drop measures for ruptures with heterogeneous stress change and implications for earthquake physics. *Geophys. J. Int.* **193**, 1691–1712 (2013).
29. A. Venkataraman, H. Kanamori, Observational constraints on the fracture energy of subduction zone earthquakes. *J. Geophys. Res.* **109**, B05302 (2004).
30. L. Ye, T. Lay, H. Kanamori, L. Rivera, Rupture characteristics of major and great ($M_w \geq 7.0$) megathrust earthquakes from 1990 to 2015: 1. Source parameter scaling relationships. *J. Geophys. Res.* **121**, 826–844 (2016).
31. A. Leith, J. A. Sharpe, Deep-focus earthquakes and their geological significance. *J. Geol.* **44**, 877–917 (1936).
32. C. Frohlich, Aftershocks and temporal clustering of deep earthquakes. *J. Geophys. Res.* **92**, 13944–13956 (1987).
33. M. J. Bezada, E. D. Humphreys, Contrasting rupture processes during the April 11, 2010 deep-focus earthquake beneath Granada, Spain. *Earth Planet. Sci. Lett.* **353–354**, 38–46 (2012).
34. M. Sambridge, Geophysical inversion with a neighbourhood algorithm—I. Searching a parameter space. *Geophys. J. Int.* **138**, 479–494 (1999).
35. Y. Xu, K. D. Koper, O. Sufri, L. Zhu, A. R. Hutko, Rupture imaging of the $M_w$ 7.9 12 May 2008 Wenchuan earthquake from back projection of teleseismic *P* waves. *Geochem. Geophys. Geosys.* **10**, Q04006 (2009).
36. J. C. VanDecar, R. S. Crosson, Determination of teleseismic relative phase arrival times using multi-channel cross-correlation and least squares. *Bull. Seismol. Soc. Am.* **80**, 150–159 (1990).
37. H. Hartzell, T. H. Heaton, Inversion of strong ground motion and teleseismic waveform data for the fault rupture history of the 1979 Imperial Valley, California, earthquake. *Bull. Seismol. Soc. Am.* **73**, 1553–1583 (1983).
38. M. Kikuchi, H. Kanamori, Note on teleseismic body-wave inversion program; wwweic.eri.u-tokyo.ac.jp/ETAL/KIKUCHI/.
39. C. L. Lawson, R. J. Hanson, *Solving Least Squares Problems* (Society for Industrial and Applied Mathematics, Philadelphia, PA, 1995).
40. G. P. Hayes, D. J. Wald, R. L. Johnson, Slab 1.0: A three-dimensional model of global subduction zone geometries. *J. Geophys. Res.* **117**, B01302 (2012).


**Acknowledgments:** The IRIS-DMC provided all of the seismic recordings. We thank three anonymous reviewers for their thoughtful comments. **Funding:** This work was supported in part by NSF grant EAR-1245717 (T.L.) and by the Initiative d'Excellence (IDEX) funding framework (Université de Strasbourg) and the CNRS international program for scientific cooperation (PICS) (Z.D.). **Author contributions:** L.Y. performed the teleseismic body-wave analysis. Z.D. performed the two-event W-phase analysis. L.Y., T.L., H.K., Z.Z., and Z.D. contributed to the interpretation and writing of the article. **Competing interests:** The authors declare that they have no competing interests. **Data and materials availability:** All of the raw waveform data are openly available from the Data Management System of IRIS. Other data needed to evaluate the conclusions in the paper are present in the paper and/or the Supplementary Materials. Additional data related to this paper may be requested from the authors.

Submitted 18 March 2016
Accepted 31 May 2016
Published 24 June 2016
10.1126/sciadv.1600581

**Citation:** L. Ye, T. Lay, H. Kanamori, Z. Zhan, Z. Duputel, Diverse rupture processes in the 2015 Peru deep earthquake doublet. *Sci. Adv.* **2**, e1600581 (2016).

ScienceAdvances
AAAS

**Diverse rupture processes in the 2015 Peru deep earthquake doublet**

Lingling Ye, Thorne Lay, Hiroo Kanamori, Zhongwen Zhan and Zacharie Duputel (June 24, 2016)

*Sci Adv* 2016, 2:.
doi: 10.1126/sciadv.1600581

Science Advances

AAAS

advances.sciencemag.org/cgi/content/full/2/6/e1600581/DC1

# Supplementary Materials for

## Diverse rupture processes in the 2015 Peru deep earthquake doublet

Lingling Ye, Thorne Lay, Hiroo Kanamori, Zhongwen Zhan, Zacharie Duputel

Published 24 June 2016, *Sci. Adv.* **2**, e1600581 (2016)
DOI: 10.1126/sciadv.1600581

**This PDF file includes:**

- fig. S18. The product of $V_r^3 \Delta\sigma_E$ for the 2015 Peru deep doublet events E1 and E2.
- fig. S19. Direct comparison of seismic radiation of the 2015 Peru deep doublet events E1 and E2.
- Legends for movies S1 and S2

**Other Supplementary Material for this manuscript includes the following:**
(available at advances.sciencemag.org/cgi/content/full/2/6/e1600581/DC1)

- movie S1 (.mov format). Animation of back-projections of 0.1- to 1.0-Hz *P* waves for the global station distribution and NA-EU wide-aperture network (NA) for E1.
- movie S2 (.mov format). Animation of back-projections of 0.1- to 1.0-Hz *P* waves for the global station distribution and NA-EU wide-aperture network (NA) for E2.

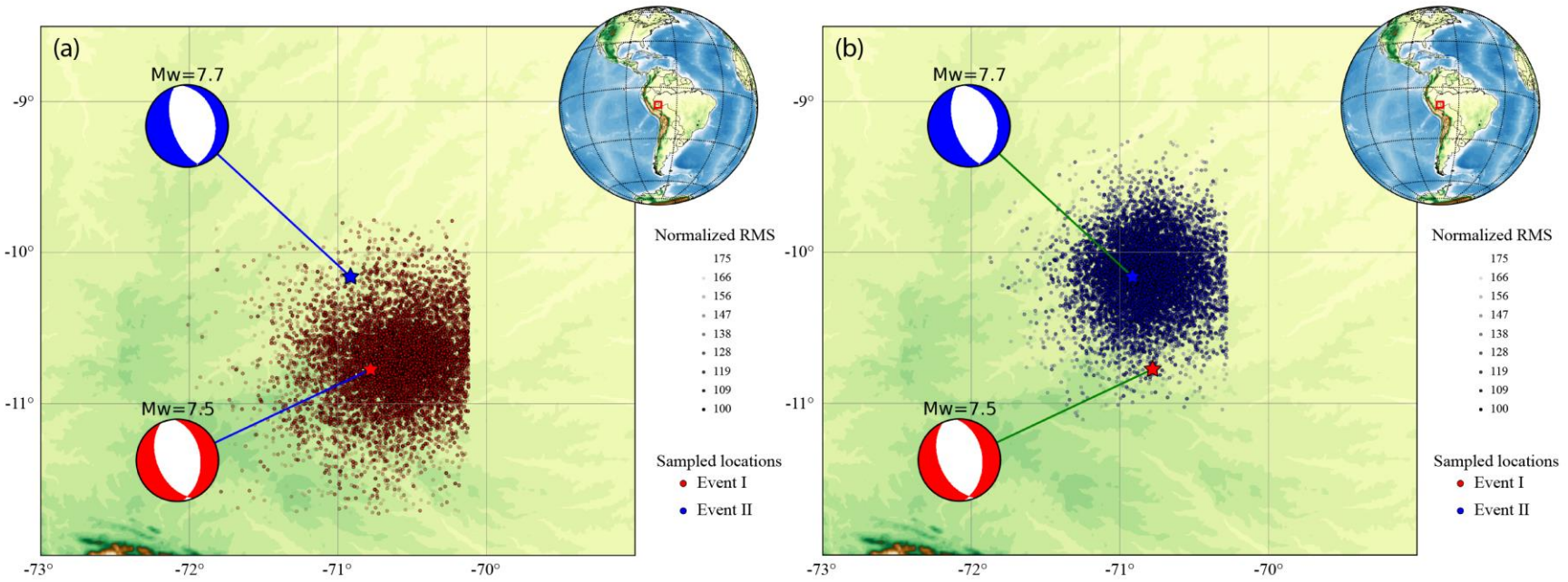


**fig. S1. Two–point-source W-phase inversion results for the 2015 Peru earthquake doublet.** (**a**) The suite of sampled hypocentral locations for E1 along with the optimal best-double couples for E1 and E2 found in the two-event W-phase inversion. (**b**) The suite of sampled hypocentral locations for E2. A modified version of the Neighborhood Algorithm sampler (*35*) was used. The transparency of the colored symbols increases with the RMS misfit normalized by the minimum value. The red and blue stars indicate the corresponding optimum centroid locations.

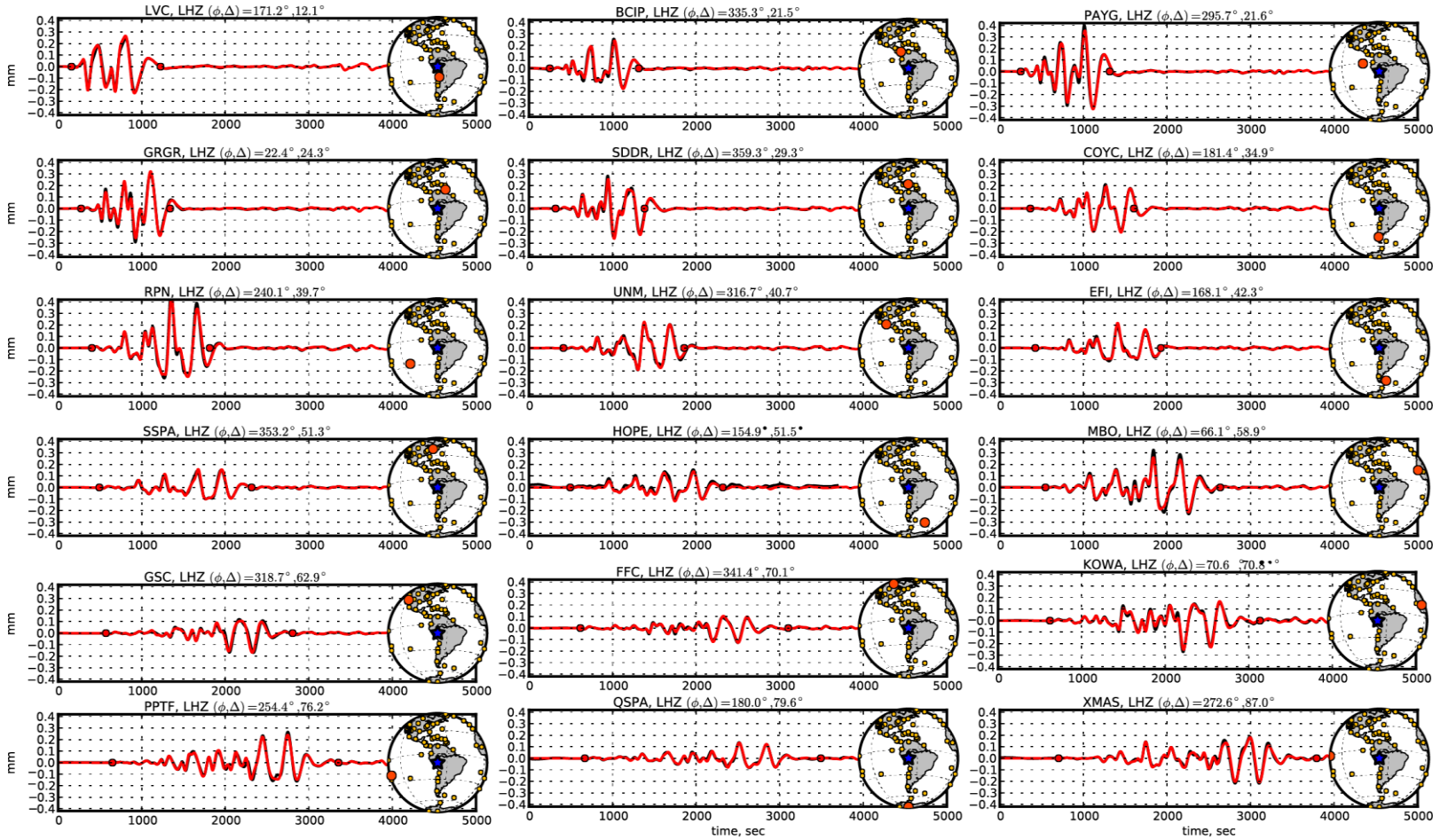


**fig. S2. Long-period waveform comparisons for the 2015 Peru earthquake doublet.** Examples of observed ground displacement waveforms (black lines) and corresponding synthetics (red lines) computed from the optimal two-point source W-phase inversion. The station azimuth (φ) and epicentral distance (Δ) are given. The time-window used in the inversion is bounded by red dots. The inset maps show the locations of all stations used with gold circles, with the specific station for the waveform shown being indicated in red. The blue stars are the locations of the doublet.

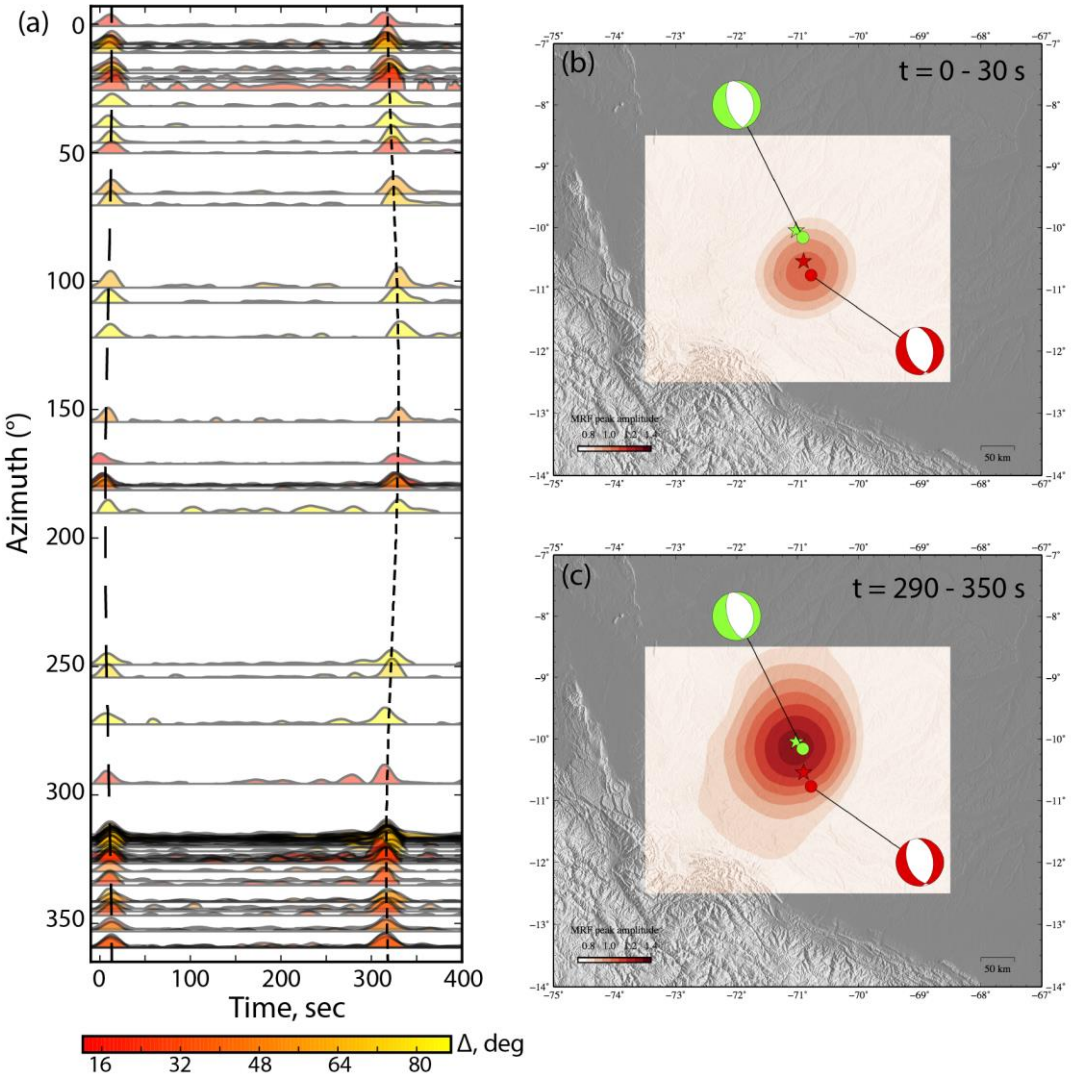


**fig. S3. Rayleigh wave MRFs for the 2015 Peru earthquake doublet.** (**a**) Rayleigh wave MRFs estimated by correcting for propagation effects plotted as a function of azimuth and colored by epicentral distance (Δ). Centroid location shifts can be inferred from the azimuthal variations in relative timing of the MRF peaks, as tracked with black dashed lines. (**b**) and (**c**) Peak stacked energy of MRFs back-projected to a gridded region around the epicenters (stars) showing the estimated centroid locations from the long-period surface wave energy. The best-double couples from the two-event W-phase inversion for E1 (red) and E2 (green) are shown with stacks for back-projection time windows spanning each event.

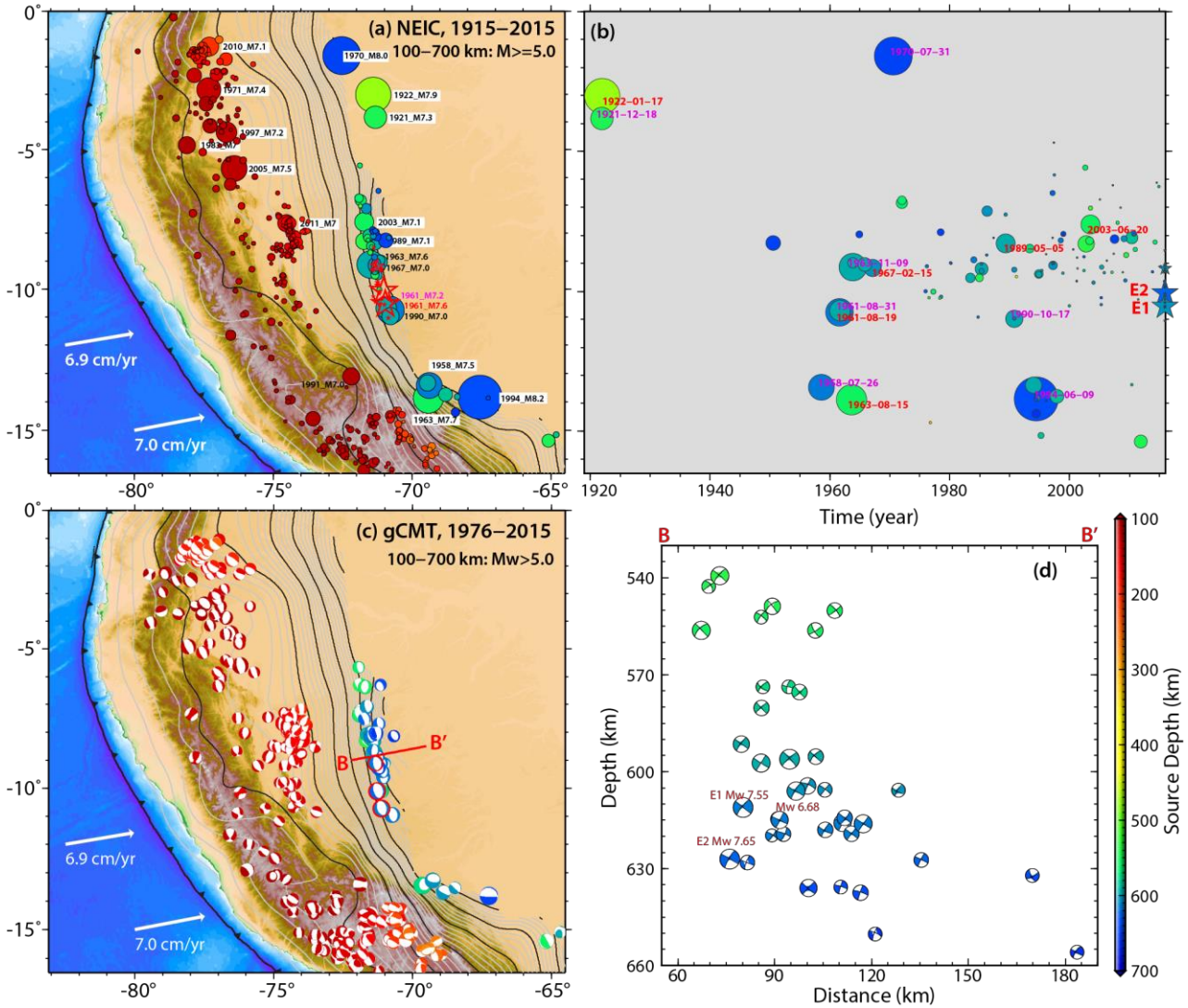


**fig. S4. Historical earthquakes around the 2015 Peru deep doublet**. (**a**) Seismicity in the slab sinking below Peru with magnitude ≥ 5.0 and source depth ≥ 100 km between 1915 and 2015 from the USGS/NEIC catalog. Circles are color-coded by event depth and scaled in radius proportional to seismic magnitude. The red stars show the epicenter of the 2015 Peru deep doublet and its aftershock sequence. (**b**) The latitude-time distribution of deep (300 to 700 km) seismicity in (a) with symbols color-coded for event depth and scaled in radius proportion to seismic magnitude. Dates are indicated for events with magnitudes larger than 7.0. (**c**) All moment tensor solutions from the global Centroid-Moment Tensor catalog from 1976-2015 for depths ≥ 100 km, with compressional quadrants color-coded for source depth and radius scaled proportional to moment magnitude. (**d**) Cross-section of the deep CMT focal mechanisms along profile B-B' in (c) viewed from the horizontal perpendicular direction. The black and gray contours in (a) and (c) show the slab surface depth with 100 km and 20 km intervals, respectively. The white vectors indicate the Nazca plate motion velocities relative to a fixed South American Plate.

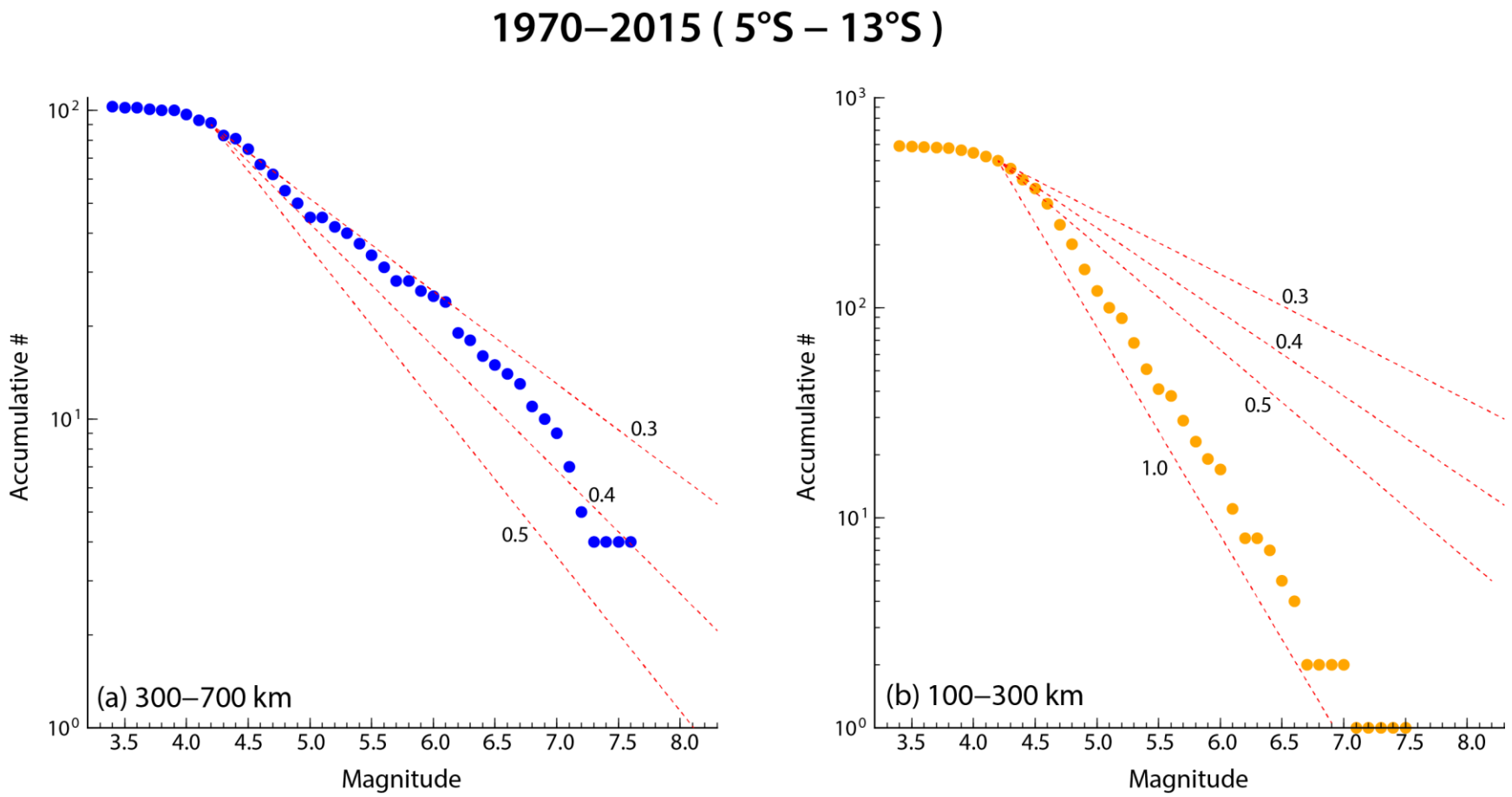


**fig. S5. Gutenberg-Richter plots for intra-slab seismicity beneath Peru**. The number of (**a**) deep-focus and (**b**) intermediate-depth earthquakes larger than a given magnitude versus magnitude for the latitude range 5°S to 13°S beneath Peru (fig. S4) for time period 1970 to 2015 from the USGS/NEIC catalog. The dashed lines indicated reference slopes (b-values). For deep-focus earthquakes in this region, the b-value is around 0.3-0.4 (a), whereas the b-value is close to 1 for intermediate-depth earthquakes in this region (b).

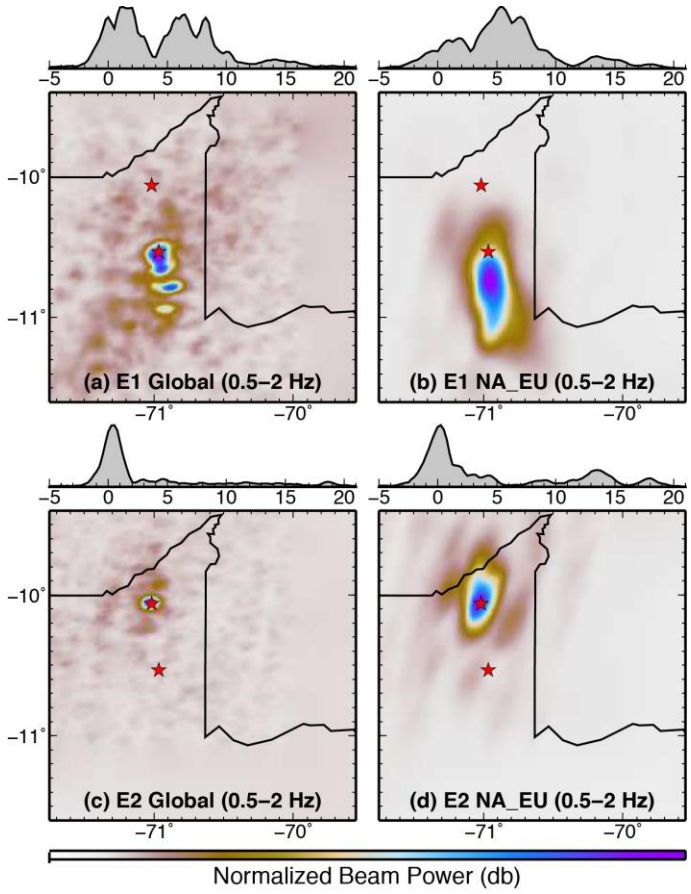


**fig. S6. Constraints on rupture dimension and rupture velocity from *P*-wave back-projections.** Teleseismic P waves in the frequency band from 0.5 to 2.0 Hz from a global distribution of stations and from North American and Europe networks (NA_EU) were used to image the coherent seismic radiation from events E1 (**a**), (**b**) and E2 (**c**), (**d**). The time-integrated back-projected signal power over a grid around the source, at its hypo central depths respectively, is shown relative to the mainshock epicenters (red stars). For E1, both global and NA_EU images indicate southward rupture extent over a distance > 50 km with a rupture propagation speed of ~4.5 km/s. Both images for E2 indicate spatially concentrated radiation without clear rupture expansion with time.

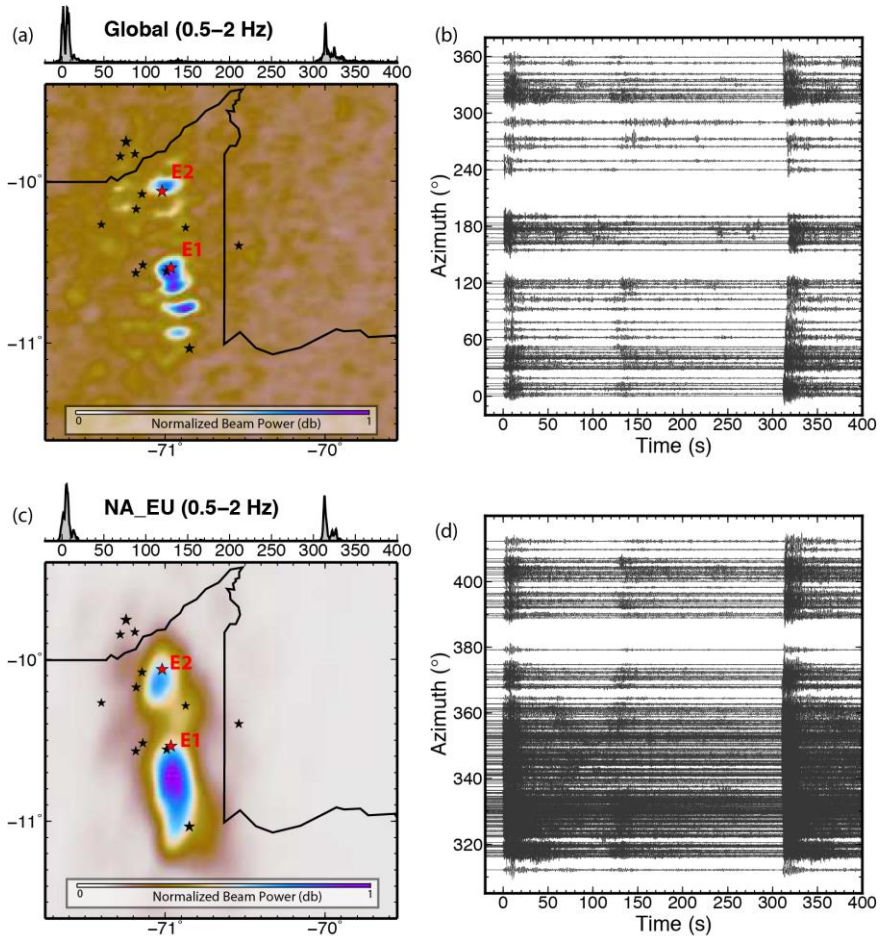


**fig. S7. A 400s-window *P*-wave back-projection for the 2015 Peru deep doublet.** Time-integrated back-projection of 0.5 to 2.0 Hz P wave beam power distributions from global (a) and NA_EU (c) networks are shown over a grid spanning both E1 and E2 at the source depth of E1. Red stars indicate the event epicenters. The time varying peak beam power is shown above each image. The black stars indicate locations of aftershocks. The corresponding filtered P waves from global (b) and NA_EU (d) networks aligned on the onset of event E1 plotted as a function of azimuth from the source region.

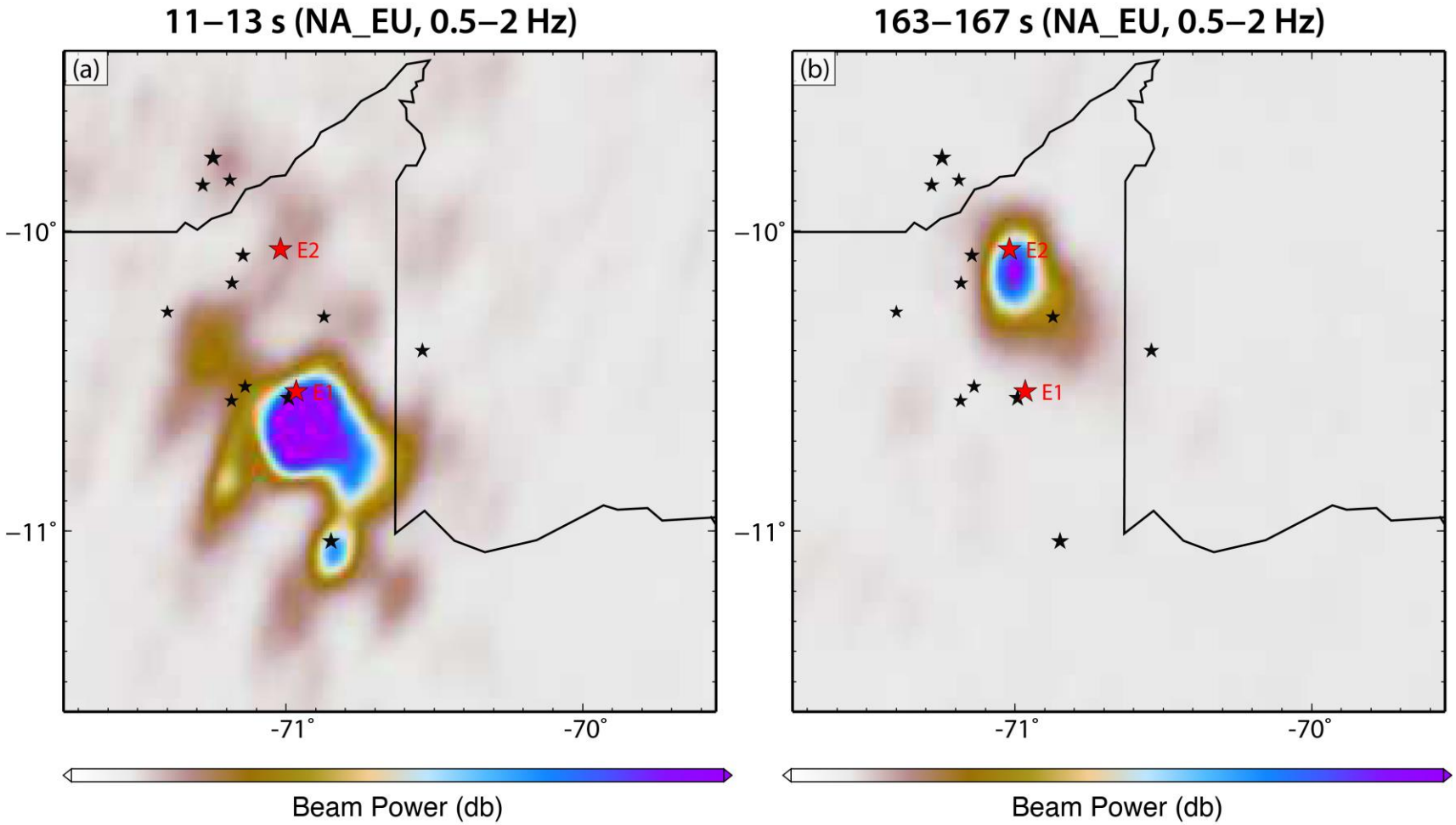


**fig. S8. Evidence for coseismic dynamic triggering by E1 and early small earthquake at the location of E2.** The time-integrated beam power for back-projection of 0.5 – 2 Hz teleseismic P waves from NA_EU network at (**a**) 11 – 13 s and (**b**) 163 – 167 s.

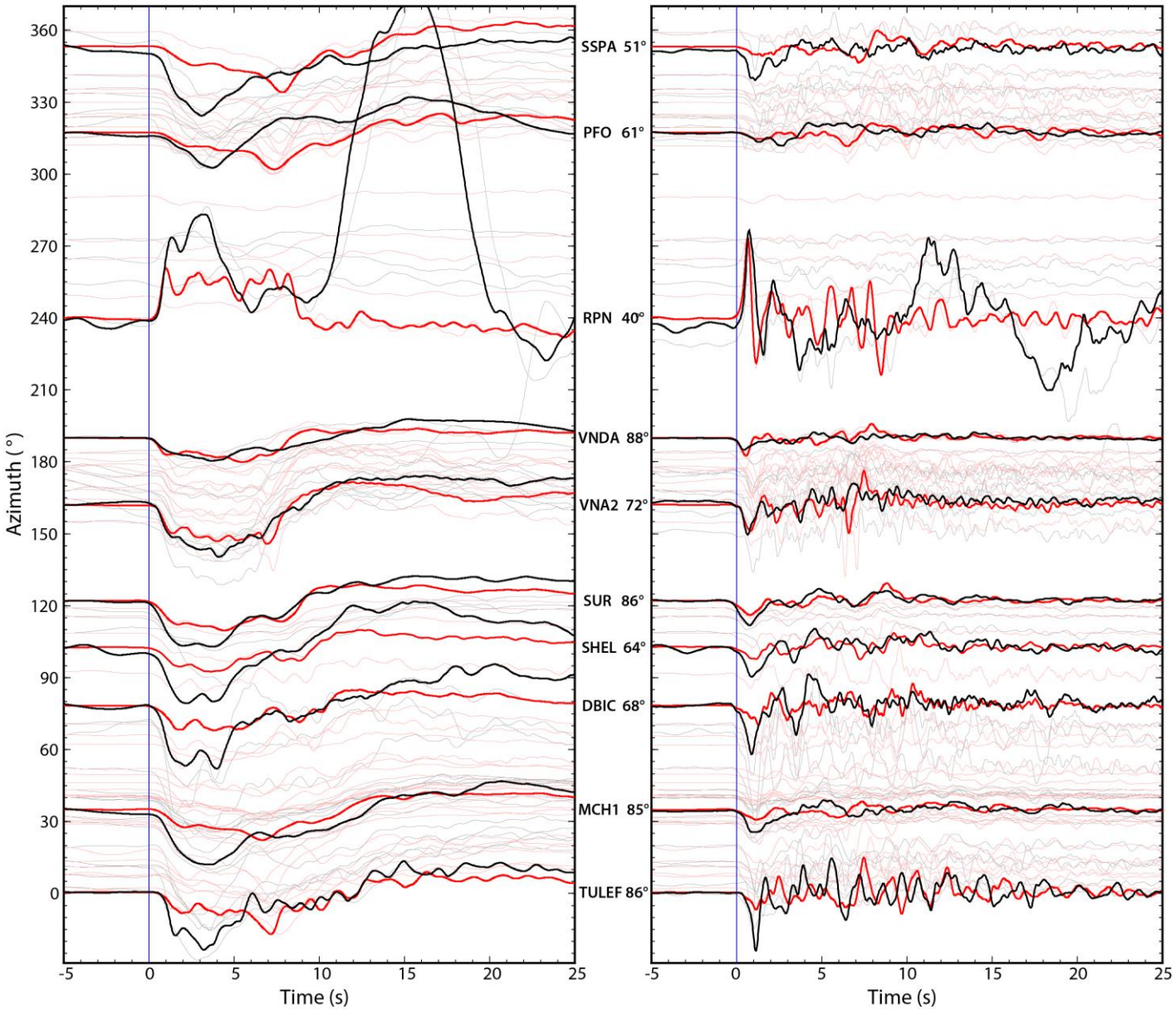


**fig. S9. Comparison of teleseismic waveforms of E1 and E2.** Ground displacement waveforms (left) and ground velocity waveforms (right) are plotted with true relative amplitudes for E1 (red traces) and E2 (black traces) as a function of azimuth from the source. Sample waveforms from labeled stations are shown in solid lines, and all other recordings are shown in faded lines. The large secondary arrival in the E2 waveform at RPN is the S arrival from E1.

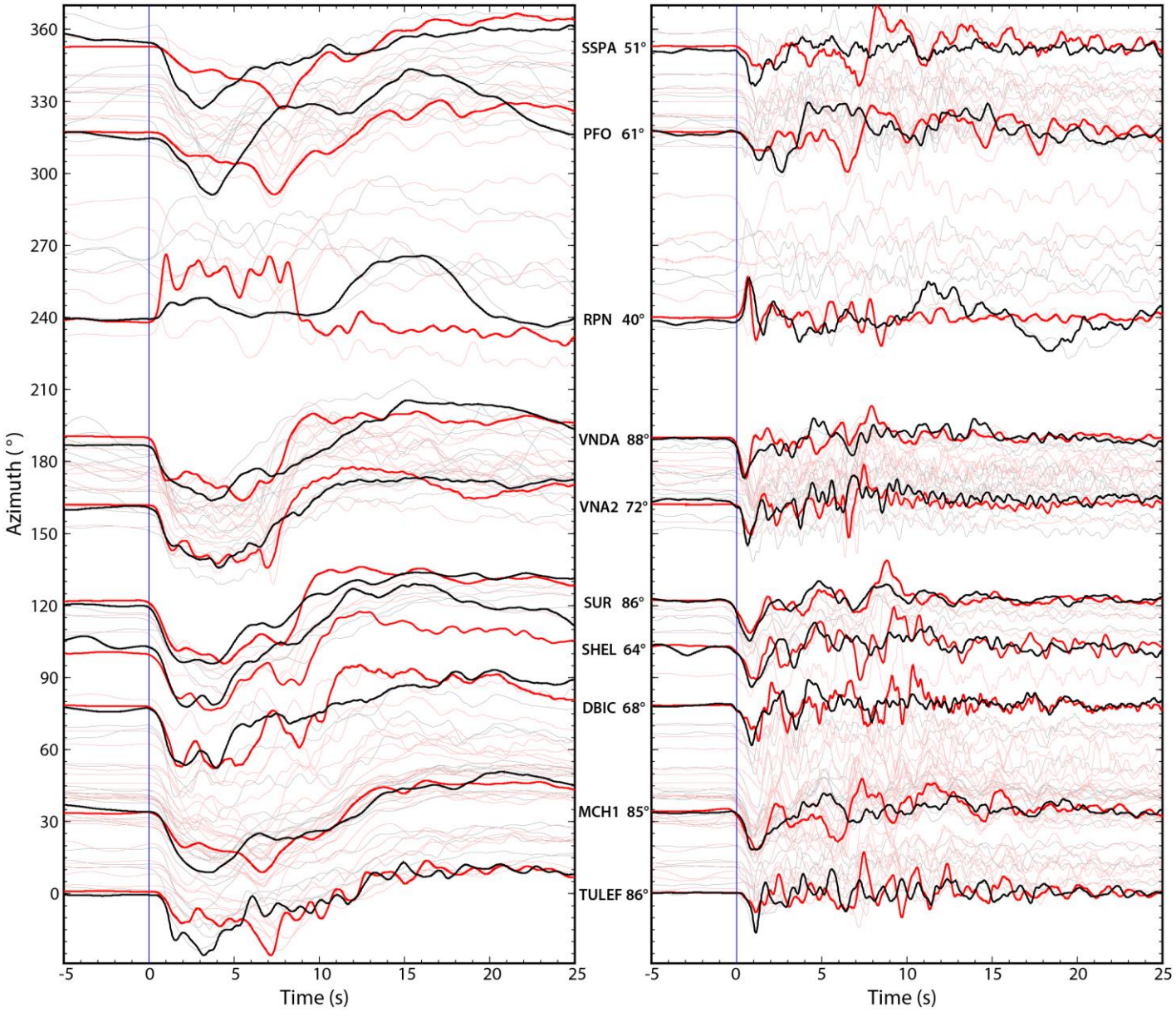


**fig. S10. Comparison of teleseismic waveforms of E1 and E2.** Ground displacement waveforms (left) and ground velocity waveforms (right) are plotted with self-normalized amplitudes for E1 (red traces) and E2 (black traces) as a function of azimuth from the source. Sample waveforms from labeled stations are shown in solid lines, and all other recordings are shown in faded lines.

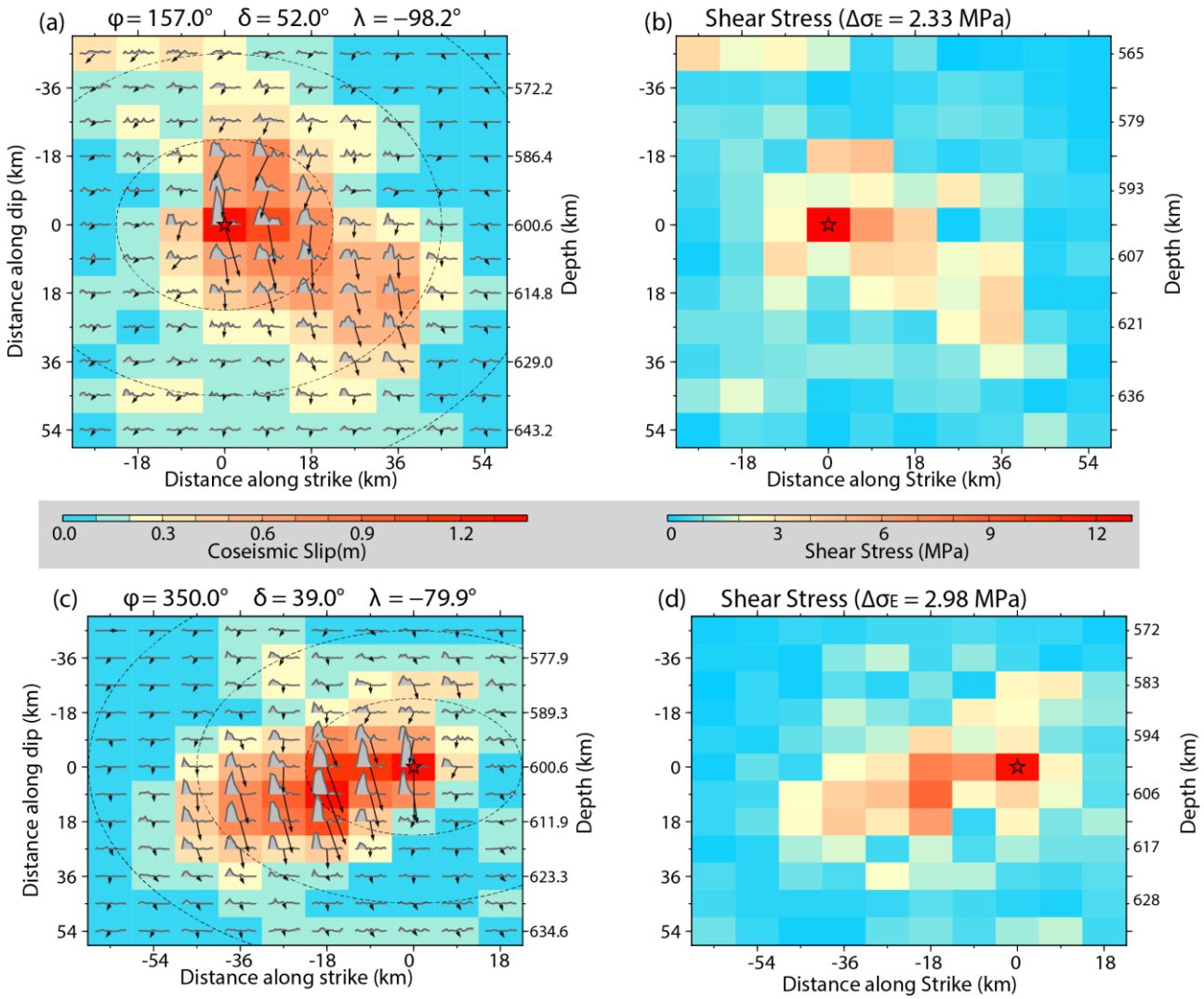


**fig. S11. Finite-fault slip models and shear stress changes for Peru event E1**. These models are for the westward (**a**, **b**) and eastward (**c**, **d**) dipping fault planes with indicated strike (ϕ), dip (δ) and average rake (λ), using the preferred rupture speed of 4.5 km/s and grid spacing of 9 km. Slip models (a, c) show the subfault source time functions and average slip magnitude (color scale and vector length) and direction (vector orientation in the fault-plane coordinate system). The dashed lines indicate the rupture front in 5 s intervals. (b) Shear stress distributions (b, d) are calculated at the subfault mid-points for the variable slip distributions. The average stress drops $\Delta\sigma_E$, weighted by the slip distribution (*29*) are 2.33 MPa and 3.0 MPa.

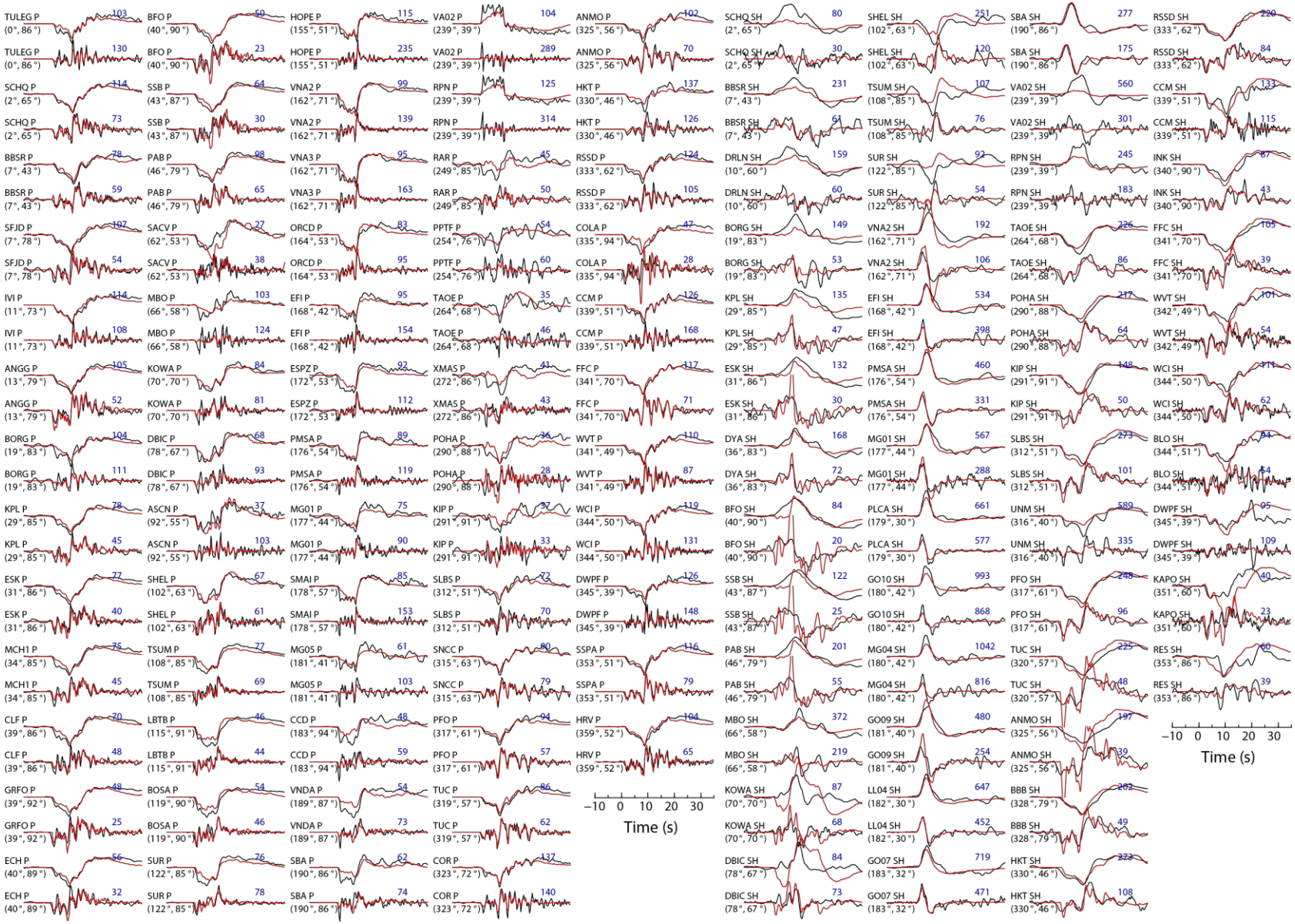


**fig. S12. Observed and predicted waveforms for event E1 on the westward dipping fault plane (strike 157°).** Observed (black lines) and modeled (red lines) broadband P and SH waveforms. The synthetic waveforms are for the finite-fault model in figs. 1 and S11a. For each station, both displacement (first) and velocity (second) waveforms are shown, the station azimuths and epicentral distances are indicated, along with the peak-to-peak amplitudes in microns or microns/s (blue numbers).

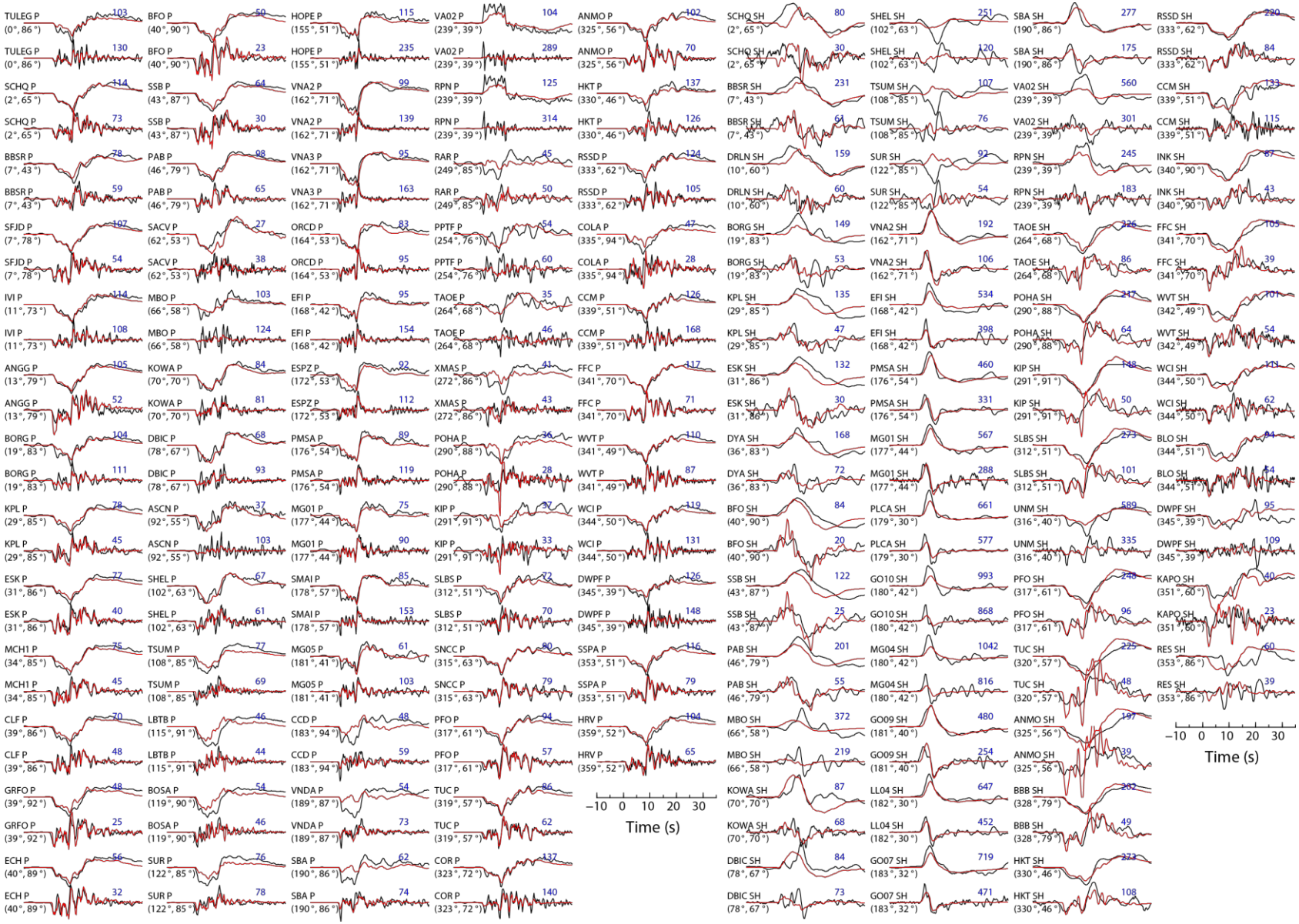


**fig. S13. Observed and predicted waveforms for E1 on the eastward dipping fault plane (strike 350°).** Observed (black lines) and modeled (red lines) broadband P and SH waveforms. The synthetic waveforms are for the finite-fault model in fig. S131c. For each station, both displacement (first) and velocity (second) waveforms are shown, the station azimuths and epicentral distances are indicated, along with the peak-to-peak amplitudes in microns or microns/s (blue numbers).

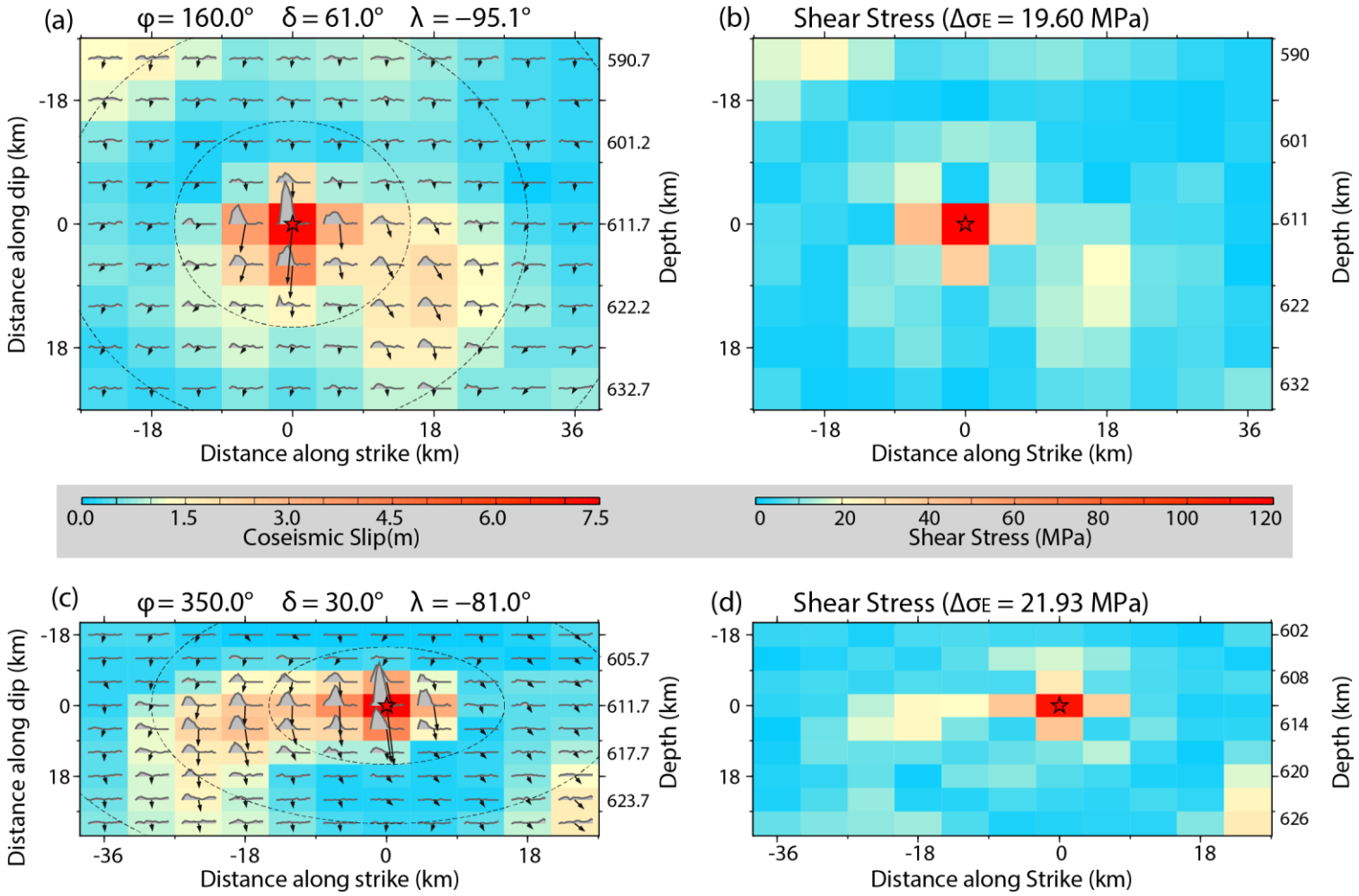


**fig. S14. Finite-fault slip models and shear stress changes for Peru E2**. These models are for the westward (**a**, **b**) and eastward (**c**, **d**) dipping fault planes with indicated strike (ϕ), dip (δ) and average rake (λ), using the preferred rupture speed of 3.0 km/s and grid spacing of 9 km. Slip models (a, c) show the subfault source time functions and average slip magnitude (color scale and vector length) and direction (vector orientation in the fault-plane coordinate system). The dashed lines indicate the rupture front in 5 s intervals. (b) Shear stress distributions (b, d) are calculated at the subfault mid-points for the variable slip distributions. The average stress drops $\Delta\sigma_E$, weighted by the slip distribution (29) are 19.6 MPa and 21.9 MPa.

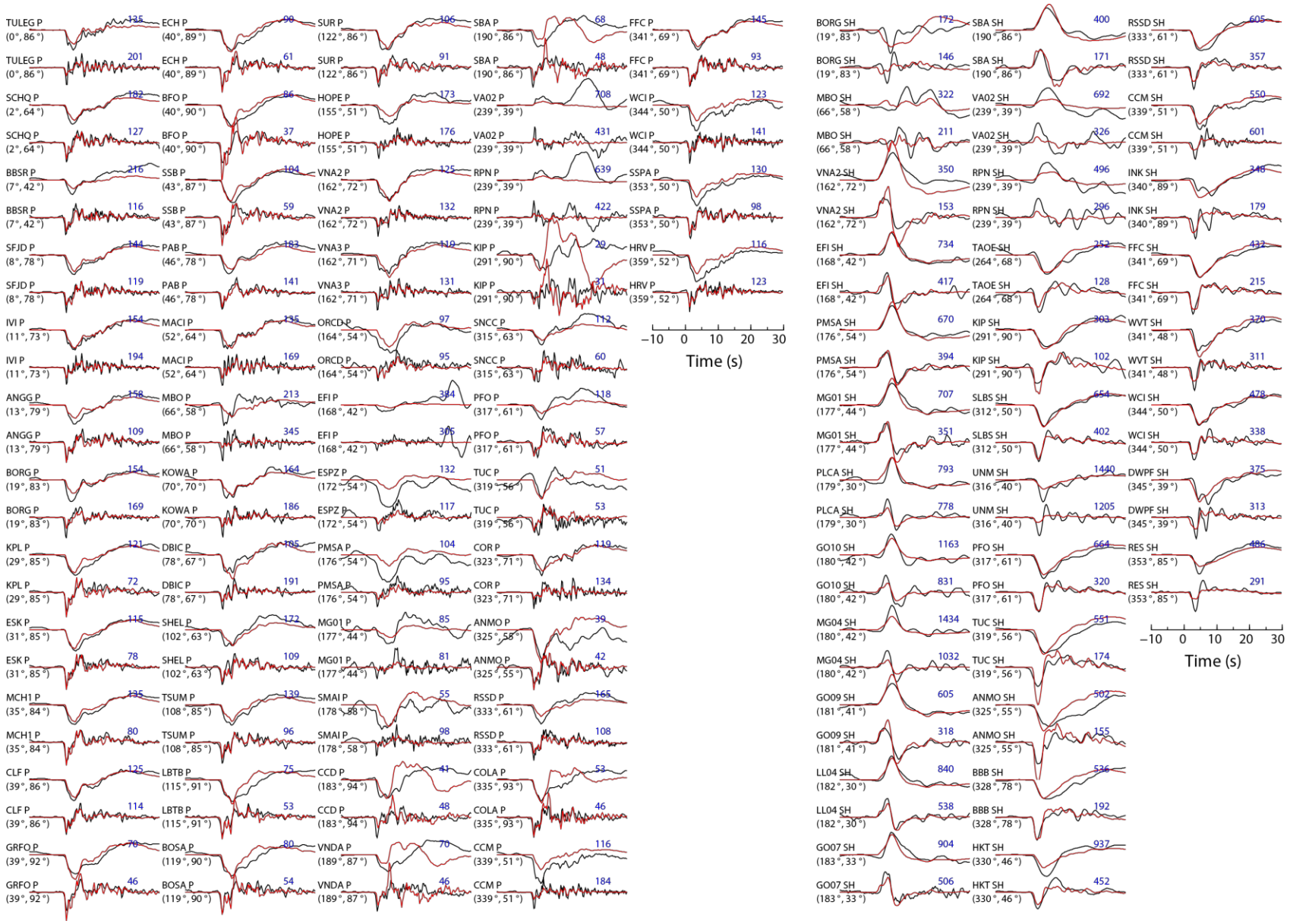


**fig. S15. Observed and predicted waveforms for E2 on the westward dipping fault plane (strike 160°).** Observed (black lines) and modeled (red lines) broadband P and SH waveforms. The synthetic waveforms are for the finite-fault model in figs. 1 and S14a. For each station, both displacement (first) and velocity (second) waveforms are shown, the station azimuths and epicentral distances are indicated, along with the peak-to-peak amplitudes in microns or microns/s (blue numbers).

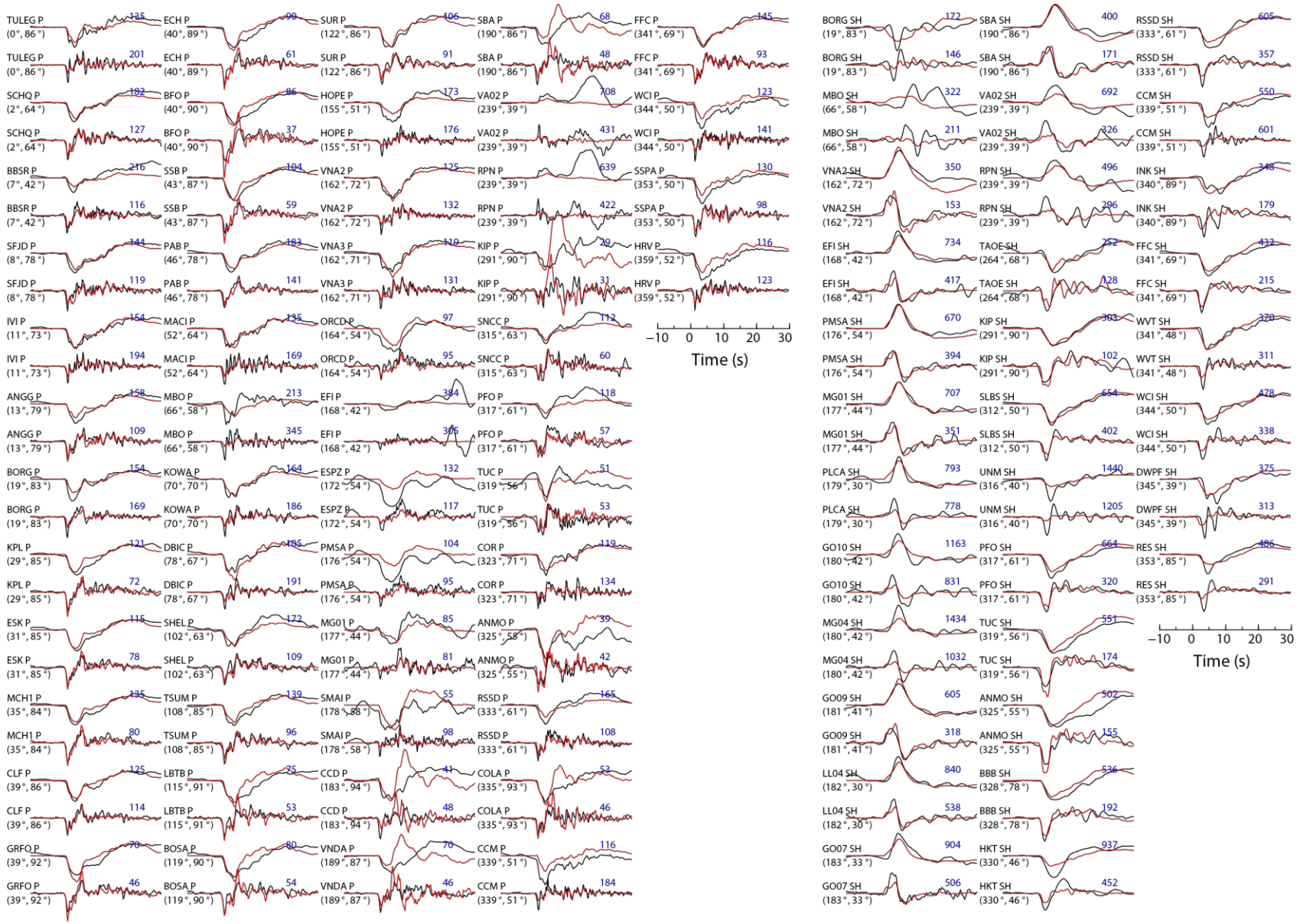


**fig. S16. Observed and predicted waveforms for E2 on the eastward dipping fault plane (strike 350°).** Observed (black lines) and modeled (red lines) broadband P and SH waveforms. The synthetic waveforms are for the finite-fault model in fig. S14c. For each station, both displacement (first) and velocity (second) waveforms are shown, the station azimuths and epicentral distances are indicated, along with the peak-to-peak amplitudes in microns or microns/s (blue numbers).

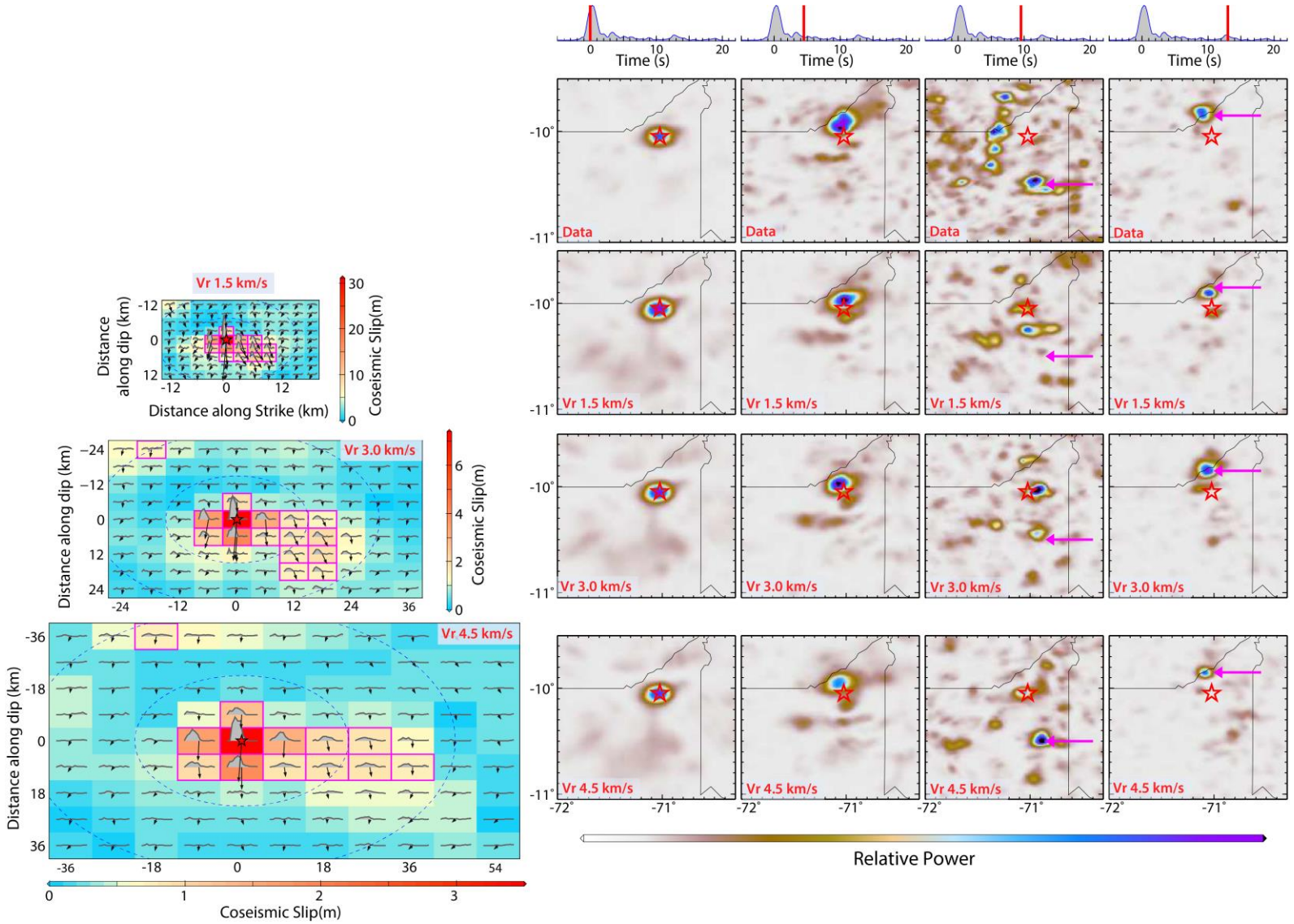


**fig. S17. Comparison of back-projections for data and synthetics from inverted slip models with different rupture speeds for E2**. Four snapshots of time-integrated back-projection images at 0 sec, 3-4 s, 8-10 s, and 12-13 s are shown for global 0.1-1 Hz data and synthetics for three slip models (left panels) with assumed rupture expansion speeds of 1.5 km/s, 3 km/s and 4.5 km/s. Coherent features at 8-10 s and 12-13 s to the south and north of the epicenter (red star), respectively, are highlighted by red arrows. This secondary radiation is too close to the epicenter for the model with $V_r$ = 1.5 km/s compared with the data images. An additional weak feature (question mark) further to the south at 8-10 s from $V_r$ 4.5 km/s does not exist in the data image. The feature at 12-13 s has an apparent velocity from the hypocenter of 3 km/s. Thus, we prefer the slip model for $V_r$ 3.0 km/s, as an overall average rupture expansion velocity.

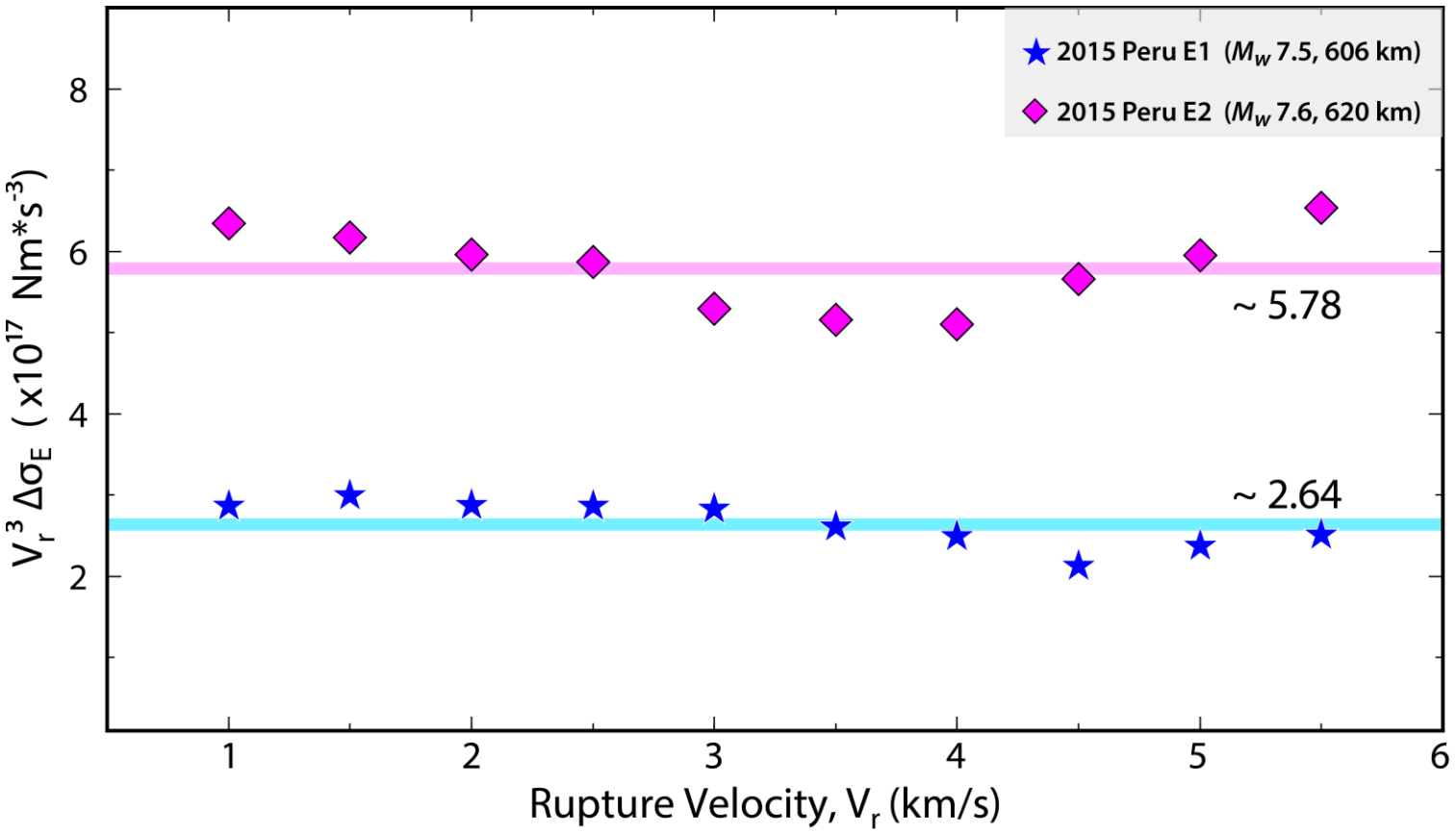


**fig. S18. The product of $V_r^3\Delta\sigma_E$ for the 2015 Peru deep doublet events E1 and E2.** The static stress drop $\Delta\sigma_E$ is estimated from the finite-fault slip model with assumed rupture expansion velocity $V_r$. Although $V_r$ and $\Delta\sigma_E$ cannot be constrained well individually, the product $\boldsymbol{V_r^3\Delta\sigma_E}$ can be constrained well by slip inversion, as there is little variation with assumed $V_r$ for either E1 or E2. The cyan and magenta lines show the logarithmic averages of 2.64 x $10^{17}$ Nm/s$^3$ and 5.78 x $10^{17}$ Nm/s$^3$ for E1 and E2 respectively. A factor of ~ 2 difference between E1 and E2 is consistent with the product of $\eta_R V_r^{-3}$ shown in Fig. 5.

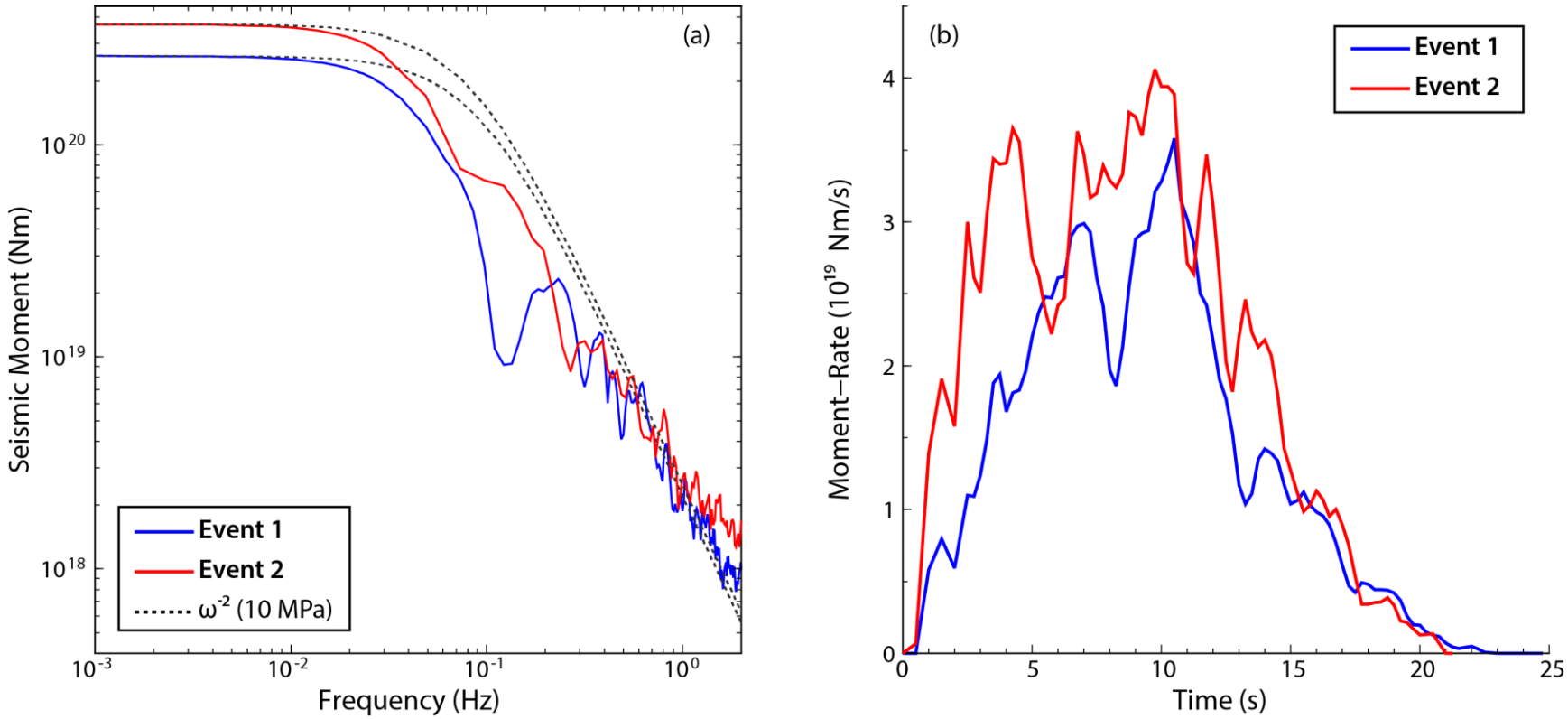


**fig. S19. Direct comparison of seismic radiation of the 2015 Peru deep doublet events E1 and E2.** (**a**) Broadband source spectra obtained from rupture slip models for frequencies below 0.05 Hz and averages of teleseismic P wave spectra for higher frequencies, and (**b**) moment-rate functions are shown for the 2015 Peru E1 (blue) and E2 (red). The dashed lines in (a) are reference ω-square spectra with a 10 MPa stress parameter and shear wave speed of 5.6 km/s. The trough near 0.1 Hz in the source spectrum of E1 results from the unilateral rupture boxcar-type teleseismic displacements in figs. S12 and S13. The moment-rate functions in (b) are from the finite-fault slip models shown in figs. 1, S11a, and S14a.

**movie S1.** Animation of back-projections of 0.1- to 1.0-Hz *P* waves for the global station distribution and NA-EU wide-aperture network (NA) for E1. The peak beam power at each time step is shown in the time series at the top with a marker that tracks time into the image. The map below shows the fourth-root relative beam power at each source grid position as a function of time. The star indicates the epicentral location. Power ranges from zero (white) to peak normalized value of 1 (magenta).

**movie S2.** Animation of back-projections of 0.1- to 1.0-Hz *P* waves for the global station distribution and NA-EE wide-aperture network (NA) for E2. The peak beam power at each time step is shown in the time series at the top with a marker that tracks time into the image. The map below shows the fourth-root relative beam power at each source grid position as a function of time. The star indicates the epicentral location. Power ranges from zero (white) to peak normalized value of 1 (magenta).